Capillary wave motion excited by high frequency surface acoustic waves

Ming K. Tan,[1] James R. Friend,[1] Omar K. Matar,[2] and Leslie Y. Yeo[1,a)]

[1]*Department of Mechanical and Aerospace Engineering, Micro/Nanophysics Research Laboratory, Monash University, Clayton, Victoria 3800, Australia and The Melbourne Centre for Nanofabrication, Clayton, Victoria 3800, Australia*
[2]*Department of Chemical Engineering, Imperial College, London SW7 2AZ, United Kingdom*

This paper presents a numerical and experimental study of capillary wave motion excited by high frequency surface acoustic waves (SAWs). The objective of this study is to provide insight into the dynamic behavior of the fluid free surface and its dependence on the excitation amplitude. A two-dimensional numerical model that couples the motion of the piezoelectric substrate to a thin liquid layer atop the substrate is constructed. A perturbation method, in the limit of small-amplitude acoustic waves, is used to decompose the equations governing fluid motion to resolve the widely differing time scales associated with the high frequency excitation. While this model focuses on the free surface dynamics in the low-amplitude flow regime, the experimental study focuses on the high-amplitude flow regime. Transformation of time series data from both experiments and simulations into the frequency domain reveals that, in the low-amplitude regime, a fundamental resonant frequency and a superharmonic frequency are found in the frequency spectra. The former is found to be identical to that of the applied SAW, and the free surface displacement magnitude is comparable to that of the substrate displacement. Our numerical results also confirm previous speculation that the separation distance between two displacement antinodal points on the free surface is $\delta_{\mathrm{St}} \approx \lambda_{\mathrm{SAW}}/2$ for a film and $\delta_{\mathrm{St}} \approx \lambda_{\mathrm{f}}/2$ for a drop, where λ_{SAW} and λ_{f} denote the SAW wavelength and the acoustic wavelength in the fluid, respectively. Finally, in the high-amplitude regime, strong nonlinearities shift the acoustic energy to a lower frequency than that of the SAW; this low-frequency broadband response, quite contrary to the subharmonic half-frequency capillary wave excitation predicted by the classical linear or weakly nonlinear Faraday theories, is supported by a scaling analysis of the momentum equations. © *2010 American Institute of Physics*. [doi:10.1063/1.3505044]

I. INTRODUCTION

The actuation and manipulation of liquids in microdevices using surface acoustic waves (SAWs) offer many advantages over conventional methods. SAW devices have traditionally been utilized for a variety of applications[1] including microcentrifugation,[2,3] micromixing,[3,4] micopumping,[5,6] drop spreading and transport,[7–9] microreactors,[10–12] jet microejectors,[13] and microatomizers.[14–16] These varied applications arise because the behavior of a sessile drop on a SAW device can be dramatically changed by altering the displacement amplitude of the SAW, which is typically on the order of $\xi \sim 10^{-9}-10^{-8}$ m. At low displacement amplitude, the drop vibrates atop the substrate [see Fig. 1(a)]. However, at high displacement amplitude (above a critical Weber number), the drop elongates rapidly into a slender jet.[13] In between these two limits, the entire drop translates along the direction of the SAW propagation. Interestingly, when the drop spreads into a film of thickness comparable to or smaller than the acoustic wavelength, the vibration immediately changes form, resulting in rapid atomization,[14–16] which arises from the violent destabilization of capillary waves at the free surface.[16] SAW atomization has been used in many bioengineering processes including protein chip fabrication,[17] generation of aerosols containing proteins[18] or drugs,[19] formation of periodic polymer patterns on a substrate,[20] and the extraction of liquid, protein molecules, and yeast cells from paper through atomization.[21] With the advent of SAW atomization based processes, the understanding of the underlying physics, which gives rise to the formation of capillary waves and their subsequent breakup to produce atomized droplets, is of critical importance in order to fully explore the potential of this technique.

There has been a longstanding history of investigations involving vertical, pistonlike excitation of free surfaces. This dates back to the experiments of Michael Faraday[22] who observed a subharmonic response: the resultant capillary waves oscillate at one-half the excitation frequency. Faraday's study has since led to a body of work which has employed Mathieu-type equations in modeling the free surface response.[23–25] The possibility of a harmonic free surface response was captured by the analysis of Kumar and Tuckerman[26,27] and later observed by Müller *et al.*[28] for liquid films thinner than the viscous boundary layer.

Nevertheless, such simple harmonic and subharmonic Faraday responses were noticeably absent in the very first experiments measuring the capillary wave undulation driven by the SAW wherein the vibration source is in the form of a
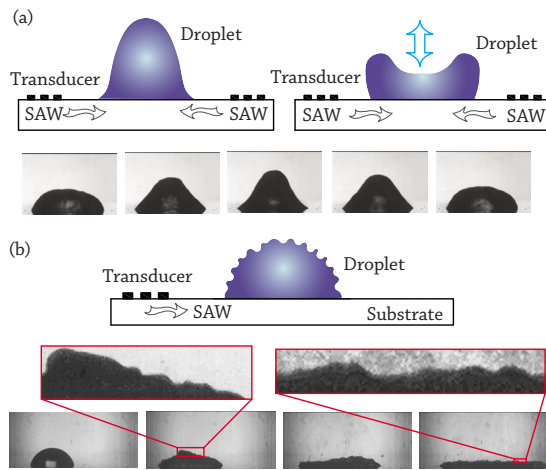
---

a)Electronic mail: leslie.yeo@monash.edu.

FIG. 1. (Color online) Schematic and experimental images showing capillary wave motion across multiple length scales: (a) apparent deformation ($\lambda_c \sim R_d$) and (b) surface deformation ($\lambda_c \ll R_d$), induced by the SAW. The experimental images in (a) were captured at 500 frames/s and indicate a drop vibration frequency around 100 Hz, whereas images in (b) were captured at 5000 frames/s. Note that the drop in (b) spreads into a thin film. Such spreading dynamics, however, is beyond the scope of the present study.
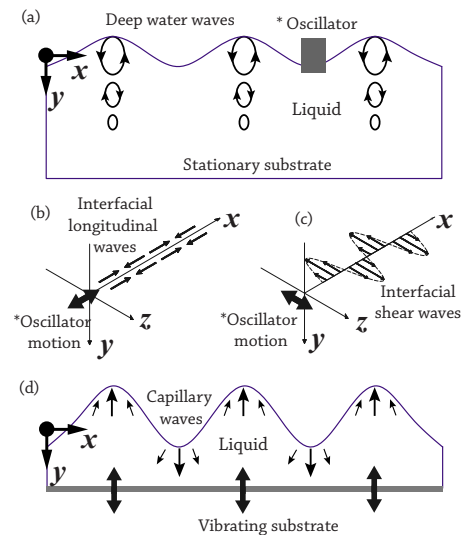

FIG. 2. (Color online) Common types of free surface deformations: (a) deep water waves, (b) interfacial longitudinal waves (Ref. 36), (c) interfacial shear waves, and (d) capillary waves. The free surface waves shown in (a)–(c) are frequently generated by introducing disturbances at the free surface using an oscillator or through the motion of a fluid layer atop the liquid-liquid interface. The free surface wave shown in (d) is generated through the excitation induced by a substrate vibrating with a pistonlike motion.

surface (Rayleigh) wave.[16] While a weak harmonic response was observed, the free surface also oscillated, quite incredibly, at frequencies some three to five orders of magnitude lower than the excitation frequency of 10^7 Hz and, furthermore, assuming a broadband nature which spanned two orders of magnitude from 10^2 to 10^4 Hz.[16] This indicates that classical Faraday-wave theory may be capable of providing only a partial explanation of the observed SAW-induced phenomena.

Further, Keolian *et al.*[29] found that period-doubling sequences far beyond the subharmonic frequencies $f \rightarrow f_0/2$ to $f_0/4$, $f_0/12$, ... $f_0/35$ were present in their Faraday-like experiment; the $f_0/35$ appeared due to an additional degree of freedom—the width of the fluid parcel—which also exhibited an influence in the period-doubling and altered the continuity of the overall period-doubling sequence. As the excitation amplitude increases, the physical appearance of additional capillary wave modes is known to occur. Since the acceleration induced by the SAW is several orders of magnitude larger than other methods in the literature and the excitation frequency itself is also several orders of magnitude higher than what is used by other investigators in the literature, it is conceivable that Qi *et al.*[16] saw an extended period-doubling of the excitation at f_{SAW} to frequencies of 10^2–10^4 Hz. Moreover, the two-dimensional and strongly curved fluid surface permits many more capillary wave modes due to three-wave resonant interaction that is perhaps best explained by Chen and Viñals[30] and Rucklidge[31] who showed the formation of patterns similar to capillary waves appearing on temporal scales remarkably different than that of the excitation signal.

With our system, beyond the SAW excitation, there is also the factor of the finite size of the drop. In general, the motion at the free surface occurs over both macroscopic and microscopic length scales.[16] In the former case, the wave-

length of the free surface waves is comparable to the drop geometry, $\lambda_c \sim R_d$, whereas in the latter, the wavelength of the free surface waves is much smaller than the drop dimension, $\lambda_c \ll R_d$. Hereafter, the former is defined as *apparent* deformations [Fig. 1(a)], and the latter is defined as *surface* deformations [Fig. 1(b)]. Depending on the disturbance or actuation mechanism, many different types of surface deformations can be formed (see Fig. 2). For a sufficiently deep liquid, the fluid elements on the free surface may follow an elliptical orbit[32] with characteristics similar to the SAW traveling on a piezoelectric substrate [see Fig. 2(a)]. Longuet-Higgins[33] investigated the instabilities of deep water irrotational gravity waves as a result of superharmonic and subharmonic[34] resonances. In addition to deep water waves, interfacial longitudinal waves[35,36] or interfacial shear waves[37] can be generated by placing an oscillator that vibrates along the *x*- or *y*-directions at the free surface, as shown in Figs. 2(b) and 2(c), respectively. The interfacial longitudinal wave motion is associated with the elastic (compression) modulus of the free surface,[35,36] while the interfacial shear wave motion is associated with the shear modulus of the free surface.[37] We note that some aspects of the Faraday instability can be understood through the framework of a Rayleigh–Taylor[38] analogy[39–41] although this is beyond the scope of the present work.

Whether driven by pistonlike vibration or the more complex vibration in the form of Rayleigh waves in the case of the SAW, the spectrum of vibrational modes present on the free surface is known to vary with a change in the displacement amplitude of the vibrating substrate.[42] More perplexing, the typical resonant response of a fluid interface with discrete resonance frequencies can give way to a broadband, chaotic response—*turbulent* capillary waves. Driving a fluid

interface at low-frequency (10^2 Hz) and high displacement amplitude, Brazhnikov et al.[43] have experimentally demonstrated that the behavior of capillary waves departs from linearity and enters into a "turbulent" capillary wave regime, exhibiting broadband power spectra in the superharmonic frequency range ($f^+ \sim 10^2 - 10^3$ Hz); some choose to describe this as *acoustic* turbulence.[44] With SAW excitation, broadband response of this sort does appear at frequencies far less than the excitation frequency, yet the broadband response appears at frequencies one to two orders of magnitude greater than the fundamental resonance frequency of the drop itself.[16] In one sense, the turbulent capillary wave response is entirely consistent with past researchers' results as the turbulence cascade appears across a broad frequency range above the drop's fundamental resonance frequency. On the other hand, the mechanism of multiple period-doubling cascades to such low-frequencies from the actual SAW excitation frequency seems to be unique to the SAW system. Given that previous studies considering broadband capillary wave excitation due to a monofrequency source have only focused on the fundamental resonant frequency f_0, however, there is no evidence of the existence of superharmonic frequencies observed on a liquid free surface to the best of our knowledge. Therefore, one of the aims of this work is to show that the superharmonic frequencies do indeed exist for the case of high-frequency SAW excitation.

Due to the difficulties in capturing the flow field beneath the free surface and measuring the complex dynamics of the free surface at fine temporal and spatial scales, experimental investigations are extremely challenging. As a result, numerical analyses have typically been used to conduct these studies. To date, numerical studies by Qi et al.,[16] Schindler et al.,[45] and Köster[46] have attempted to elucidate the mechanisms that give rise to the vibration of the free surface and the internal flow field in a drop driven by the SAW. In Qi's model, the lubrication approximation for a thin, incompressible liquid film was employed to construct a model governing the destabilization of the free surface leading toward atomization, which was solved numerically using an adaptive form of the method of lines with fourth-order centered differences for spatial discretization and an implicit Runge–Kutta scheme for time integration. To decouple the fluid-solid interaction, an analytical expression to describe a pressure disturbance imposed on the free surface that resembles the SAW, albeit with a decay in amplitude due to the energy absorbed by the fluid, was employed. This decoupling, however, omits important physics underlying how the fluid vibrates in relation to the substrate excitation.

Unlike Qi's model, the numerical studies conducted by Schindler and Köster focused on the flow field within the drop bounded by its free surface and the solid substrate. Schindler's numerical results, obtained via finite element boundary parametrization of the free surface using Galerkin discretization, successfully showed the apparent deformation of the free surface driven by SAWs and concluded that the apparent deformation of the drop was caused by the pressure force; the viscous force was far too weak to result in a substantial deformation. Nevertheless, Schindler invoked a number of questionable assumptions, including incompressibility,

steady-state flow, and a fixed body force on the fluid from the SAW, ignoring the effect of the fluid on the substrate and the determination of the actual force from the SAW on the fluid as it is generated: as a decaying, distributed body force dependent on the shape of the drop of fluid sitting on the substrate. On the other hand, Köster's approach generally follows the conventional method by using a perturbation expansion of the equations of motion for the substrate and fluid: equations at the first-order govern the propagation of linear acoustic waves and equations at the second-order (after time averaging) govern SAW streaming.[47–50] Although he was unable to resolve the surface deformation on the length scale of the capillary wave, Köster, using an arbitrary Lagrangian–Eulerian approach with second-order Taylor–Hood finite element spatial discretization and a backward Euler or Crank–Nicholson scheme for time integration, managed to capture the apparent deformation of the drop in the form of an asymmetric cone when excited from beneath by a traveling SAW, consistent with experimental observations. The complementary approach of Dong et al.,[51] in which the three-dimensional Navier–Stokes equations are solved using a volume-of-fluid method to simulate the apparent deformation of a drop subjected to lateral vibrations, demonstrates the formation of capillary waves on the drop surface. This work, which was carried out in order to analyze the effect of vibration frequency on the difference in the drop contact angles that determine the velocity of its motion along the substrate, did not account for compressibility effects and was restricted to very low vibration frequencies (of order 10^2 Hz). More recently, Brunet et al.[52] conducted a numerical study of SAW generated fluid motion in a drop with nondeformable free surface and found a "chaotic" behavior of the acoustic field within the drop as a result of multiple wave-reflection from the free surface. Brunet et al.'s finite element numerical model was based on a linear acoustic assumption and used a nondeformable stress-free surface condition to examine the acoustic field in a large hemispherical drop, i.e., $R_d > 10\lambda_f$. Due to the nondeformable free surface, their model, however, was unable to provide analysis of the surface deformation. The present work is therefore motivated by the lack of a comprehensive investigation of the dynamics of the free surface motion driven by SAW.

The rest of this paper is organized as follows. First, we construct a simple numerical model to verify the existence of high frequency capillary waves ($f_c \approx f_{\text{SAW}}$), which has yet to be captured theoretically, and also to verify the existence of superharmonic frequencies ($f^+ \sim 2f_0, 4f_0, 6f_0, \ldots$), which, to the best of our knowledge, has never been shown either theoretically or experimentally. The mathematical formulation and the numerical scheme are discussed in Sec. II. Using this model, we examine the flow field within a *film* excited by a low-amplitude SAW. In Sec. III, we report on experiments performed to investigate the relationship between the capillary frequency and the SAW amplitude, paying particular attention to the transition from low- to high-amplitude SAW. While laser Doppler vibrometry measurements of the capillary wave frequency under SAW excitation have been briefly measured in our previous work,[16] the experiments carried out here provide a more rigorous investigation of the frequency
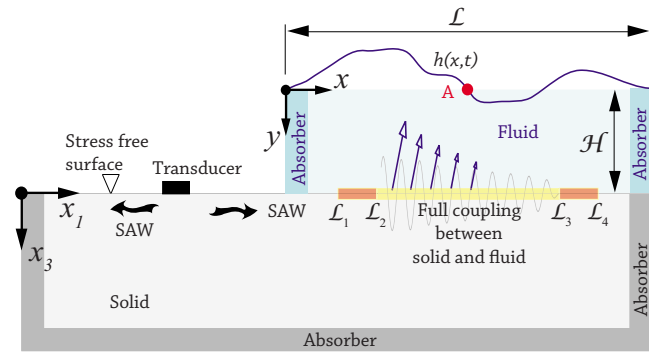
FIG. 3. (Color online) A two-dimensional schematic of the computational domain used to model the surface deformation and to analyze the flow field driven by the SAW. A liquid film of undisturbed thickness $\mathcal{H}$ is placed on top of the piezoelectric substrate. At the solid-fluid interface, the section defined by $(\mathcal{L}_2 - \mathcal{L}_3)$ represents the region of full coupling between the fluid and solid, whereas the sections defined by $(\mathcal{L}_1 - \mathcal{L}_2)$ and $(\mathcal{L}_3 - \mathcal{L}_4)$ are transition regions. Therefore, the solid-fluid interactions are restricted within the section defined by $\mathcal{L}_2 - \mathcal{L}_3$ to reduce wall effects.

spectra as a function of the excitation amplitude over a broader frequency range. Finally, in Sec. IV, we examine the acoustic field in a *drop* and provide a case study of the alignment of microparticles on the free surface of a hemispherical drop driven by an extremely low-amplitude standing-SAW ($\xi \ll 1$ nm). The prime objective of this case study is to provide a qualitative verification of the consistency between the numerical results and experimental observations.

II. NUMERICAL SIMULATION

A schematic of the flow configuration is shown in Fig. 3. The model, which will be derived below, consists of the linear piezoelectric coupling equations,[53] a set of first-order acoustic equations,[49] and a set of second-order acoustic streaming equations[50] to accommodate the time-averaged fluid flow arising from the SAW irradiation, viscous effects, and the effect of attenuation of the SAW propagation arising from the fluid present on the substrate. We adopt a similar numerical approach reported by Qi *et al.*,[16] with a few important improvements: (1) we omit the lubrication approximation, and instead use a regular perturbation expansion to decompose the governing equations such that they can be resolved separately at small and large time scales; (2) we fully capture the fluid-structural coupling by completely solving for the equation of motion in both the solid and fluid domains. The variables across the solid-fluid interface are solved simultaneously both spatially and temporally to form a fully coupled field, allowing complex fluid-solid interactions to be studied.[6] Below, we first introduce the governing equations underpinning the motion of the piezoelectric substrate and the equations that describe the acoustic streaming field. We then transform the coordinate system of the fluid domain to allow the free surface to deform in the physical space, while remaining as a fixed-grid in the computational domain. The numerical procedure used to carry out the computations, and the initial and boundary conditions imposed, are then discussed.

A. Governing equations

The time-domain constitutive equations governing the motion of a piezoelectric substrate are given by[53–55]

$$\frac{\partial D_i}{\partial t} = e_{ikl}\frac{\partial S_{kl}}{\partial t} + \epsilon^S_{ik}\frac{\partial E_k}{\partial t}, \tag{1}$$

$$\frac{\partial T_{ij}}{\partial t} = c^E_{ijkl}\frac{\partial S_{kl}}{\partial t} - e_{kij}\frac{\partial E_k}{\partial t}, \tag{2}$$

where e_{ikl} are the piezoelectric stress coefficients, ϵ^S_{ik} are the dielectric coefficients at constant strain **S**, T_{ij} are the stress components, and c^E_{ijkl} are the elastic stiffness coefficients at a constant electric displacement **D** or field **E**. Note that the first term of the electric field displacement equation, Eq. (1), arises from the relation between the electric displacement and electric field ($D_i = \epsilon_{ik}E_k$), while the first term of the stress equation, Eq. (2), arises from Hooke's law ($T_{ij} = c_{ijkl}S_{kl}$). Equations (1) and (2) take into account the piezoelectric coupling between the electrical and mechanical variables through the piezoelectric stress tensor e_{ikl}. The tensor e_{ikl} is symmetric with respect to the last two indices k and l, i.e., $e_{ikl} = e_{ilk}$, because of the symmetric strain $S_{kl} = S_{lk}$. For an orthogonal Cartesian coordinate system $i,j,k,l \in \{1,2,3\}$.

In a piezoelectric substrate, the elastic field, described by Eqs. (1) and (2), and the electromagnetic field, as defined by Maxwell's equations, are coupled. The distribution of these fields can be determined by simultaneously solving the coupled equations. However, the velocity of the electromagnetic wave is 10^5 times faster than the elastic wave. Therefore, the mechanical dynamics and its effect on the electromagnetic field generated through the piezoelectric coupling are considerably slower than the electromagnetic radiation, so much so that we can treat the electric field as being *quasistatic*. This allows us to simplify Eq. (1) based on the quasistatic assumption $\partial \mathbf{D}/\partial t = \nabla \times \mathbf{H} \approx 0$, where **H** is the magnetic field vector. Together with the infinitesimal strain-displacement relationship,

$$\frac{\partial S_{kl}}{\partial t} = \frac{1}{2}\left(\frac{\partial^2 \xi_k}{\partial x_l \partial t} + \frac{\partial^2 \xi_l}{\partial x_k \partial t}\right). \tag{3}$$

Equations (1) and (2) are then simplified into the following form:

$$\frac{\partial E_k}{\partial t} = -\frac{e_{ikl}}{\epsilon^S_{ik}}\left[\frac{1}{2}\left(\frac{\partial v_k}{\partial x_l} + \frac{\partial v_l}{\partial x_k}\right)\right], \tag{4}$$

$$\frac{\partial T_{ij}}{\partial t} = c^E_{ijkl}\left[\frac{1}{2}\left(\frac{\partial v_k}{\partial x_l} + \frac{\partial v_l}{\partial x_k}\right)\right] - e_{kij}\frac{\partial E_k}{\partial t}, \tag{5}$$

where ξ is the particle displacement and v is the velocity. Following this, Newton's second law of motion facilitates closure of Eqs. (4) and (5) to describe the basic motion of the piezoelectric solid,

$$\rho_s \frac{\partial v_j}{\partial t} = \frac{\partial T_{ij}}{\partial x_i}, \tag{6}$$

where ρ_s is the crystal mass density. Material properties—e_{ikl}, ϵ^S_{ik}, and c^E_{ijkl}—need to be transformed to the

correct orientation. We use the bond transformation principle[53] to transform these material constants from the crystal's principal axes to the 127.68° *Y*-rotated-about-*X*-cut, *X*-propagating configuration. The transformed material properties are listed in Appendix A.

In the fluid medium, the equations describing Newtonian fluid motion are those pertaining to mass and momentum conservation,[47,49]

$$\frac{\partial \rho_f}{\partial t} + \boldsymbol{\nabla} \cdot (\rho_f \mathbf{u}) = 0, \tag{7}$$

$$\rho_f \frac{\partial \mathbf{u}}{\partial t} + \rho_f (\mathbf{u} \cdot \boldsymbol{\nabla}) \mathbf{u} = -\boldsymbol{\nabla} p + \mu \nabla^2 \mathbf{u} + \mu'' \boldsymbol{\nabla} \boldsymbol{\nabla} \cdot \mathbf{u}, \tag{8}$$

where $\mathbf{u}$ is the fluid velocity, ρ_f is its density, ρ is its pressure and $\mu'' = (\mu_B + \mu/3)$, in which μ_B is the bulk viscosity and μ the shear viscosity. A thermodynamic equation of state is used to complete the above set of equations,[48,56]

$$p - p_0 = c_0^2 (\rho_f - \rho_{f0}) + \frac{1}{2} \left. \left(\frac{\partial c^2}{\partial \rho} \right) \right|_s (\rho_f - \rho_{f0})^2$$

$$+ \frac{\partial p}{\partial s} (s - s_0) + \cdots, \tag{9}$$

where c is the sound speed and s is the entropy. In the above, the subscript "0" refers to equilibrium properties associated with the ambient conditions, i.e., $\mathbf{u}_0 = 0$ m/s, $p_0 = 101$ kPa, and $\rho_{f0} = 998$ (water) kg/m³.

Assuming infinitesimally small amplitude waves, a perturbation expansion can then be used to linearize the equations. We begin by examining the dependent variables for the fluid. The perturbation expansion is carried out in powers of the small parameter $\varepsilon = \mathcal{U}_1 / c_0 \ll 1$, where $\mathcal{U}_1$ is the characteristic acoustic particle velocity. Expansions of the fluid velocity, pressure, and density field then take the form[47,49,50,57]

$$\mathbf{u} = \mathbf{u}_0 + \varepsilon \mathbf{u}_1 + \varepsilon^2 \mathbf{u}_2 + \mathcal{O}(\varepsilon^3), \tag{10}$$

$$p = p_0 + \varepsilon p_1 + \varepsilon^2 p_2 + \mathcal{O}(\varepsilon^3), \tag{11}$$

$$\rho_f = \rho_{f0} + \varepsilon \rho_{f1} + \varepsilon^2 \rho_{f2} + \mathcal{O}(\varepsilon^3), \tag{12}$$

where the subscript "1" refers to the first-order approximations and the subscript "2" refers to the second-order field. Substitution of Eqs. (10)–(12) into Eqs. (8) and (7) subsequently yields the following first-order approximations for the mass and momentum conservation equations:[47,49,50]

$$\frac{\partial \rho_{f1}}{\partial t} + \rho_{f0} (\boldsymbol{\nabla} \cdot \mathbf{u}_1) = 0 \tag{13}$$

and

$$\rho_{f0} \frac{\partial \mathbf{u}_1}{\partial t} = -\boldsymbol{\nabla} p_1 + \mu \nabla^2 \mathbf{u}_1 + \mu'' \boldsymbol{\nabla} \boldsymbol{\nabla} \cdot \mathbf{u}_1, \tag{14}$$

respectively. From Eq. (9), the first-order approximation of the equation of state for an adiabatic process[49] $(s = s_0)$ is

$$p_1 = c_0^2 \rho_{f1}. \tag{15}$$

At the next order, the fluid motion comprises a superposition of the steady-state and harmonic time-oscillating flows. The second-order approximation to the continuity [Eq. (7)] and the momentum [Eq. (8)] equations are[47,50]

$$\frac{\partial \rho_{f2}}{\partial t} + \boldsymbol{\nabla} \cdot (\rho_{f0} \mathbf{u}_2) + \boldsymbol{\nabla} \cdot (\rho_{f1} \mathbf{u}_1) = 0, \tag{16}$$

$$\rho_{f0} \frac{\partial \mathbf{u}_2}{\partial t} + \rho_{f1} \frac{\partial \mathbf{u}_1}{\partial t} + \rho_{f0} (\mathbf{u}_1 \cdot \boldsymbol{\nabla}) \mathbf{u}_1$$

$$= -\boldsymbol{\nabla} p_2 + \mu \nabla^2 \mathbf{u}_2 + \mu'' \boldsymbol{\nabla} \boldsymbol{\nabla} \cdot \mathbf{u}_2. \tag{17}$$

Rewriting Eq. (9),

$$p - p_0 = A \left[\frac{\rho_f - \rho_{f0}}{\rho_{f0}} + \frac{1}{2} \frac{B}{A} \left(\frac{\rho_f - \rho_{f0}}{\rho_{f0}} \right)^2 \right], \tag{18}$$

the second-order approximation of the equation of state then reads

$$p_2 = \frac{c_0^2}{\rho_{f0}} \left[\frac{1}{2} \frac{B}{A} \rho_1^2 + \rho_{f0} \rho_2 \right]. \tag{19}$$

In the above, A and B are the adiabatic bulk elastic modulus and nonlinear modulus given by $A = \rho_{f0} c_0^2$ and $B = \rho_{f0}^2 (\partial c^2 / \partial \rho_f)_s$, respectively.

Subsequent time-averaging $[\langle a \rangle = 1/T \int_0^T a(t) dt$, where $T = nf^{-1}$ and $n = 1, 2, 3, \ldots]$ all the terms in Eqs. (16), (17), and (19) produces the following equations:

$$\frac{\rho_2}{\partial t} + \rho_{f0} (\boldsymbol{\nabla} \cdot \mathbf{u}_2) + \boldsymbol{\nabla} \cdot \langle \rho_{f1} \mathbf{u}_1 \rangle = 0, \tag{20}$$

$$\rho_{f0} \frac{\partial \mathbf{u}_2}{\partial t} + \left\langle \rho_{f1} \frac{\partial \mathbf{u}_1}{\partial t} \right\rangle + \rho_{f0} \langle (\mathbf{u}_1 \cdot \boldsymbol{\nabla}) \mathbf{u}_1 \rangle$$

$$= -\boldsymbol{\nabla} p_2 + \mu \nabla^2 \mathbf{u}_2 + \mu'' \boldsymbol{\nabla} \boldsymbol{\nabla} \cdot \mathbf{u}_2, \tag{21}$$

$$p_2 = \frac{1}{2} \frac{c_0^2}{\rho_{f0}} \left[\frac{B}{A} \langle \rho_1^2 \rangle + 2 \rho_{f0} \rho_2 \right]. \tag{22}$$

To accommodate the deformation of the free surface at $y = 0$ (see Fig. 3), we apply the following transformation:

$$\zeta = x, \quad \eta = \frac{y - h(x, t)}{\mathcal{H} - h(x, t)}, \tag{23}$$

where $\mathcal{H}$ is the undisturbed thickness and h is the free surface displacement from its undisturbed location $y = 0$. We expand $h(x, t)$ via the following ansatz:

$$h = h_0 + \varepsilon h_1 + \varepsilon^2 h_2 + \mathcal{O}(\varepsilon^3), \tag{24}$$

where $h_0 = 0$ and $h_1 = h_2 = 0$ at $t = 0$. Substituting Eq. (24) into Eq. (23) and eliminating terms of order $\mathcal{O}(\varepsilon^3)$ and higher, we obtain

$$\eta = \eta_0 + \frac{\varepsilon}{\mathcal{H}}\left(\frac{y}{\mathcal{H}} - 1\right)h_1 + \frac{\varepsilon^2}{\mathcal{H}}\left(-h_2 + \frac{y}{\mathcal{H}}h_2 - \frac{h_1^2}{\mathcal{H}} + \frac{y}{\mathcal{H}^2}h_1^2\right),$$

(25)

where $\eta_0 \equiv y/\mathcal{H}$. Equations (23) and (25) are then substituted into Eqs. (B1)–(B6) in Appendix B, from which we obtain the following:

$$\frac{\partial}{\partial x} = \frac{\partial}{\partial \zeta} - \varepsilon\frac{\eta'}{\mathcal{H}}\frac{\partial}{\partial \eta}\frac{\partial h_1}{\partial \zeta} + \mathcal{O}(\varepsilon^2),$$

(26)

$$\frac{\partial^2}{\partial x^2} = \frac{\partial^2}{\partial \zeta^2} - \varepsilon\frac{2\eta'}{\mathcal{H}}\frac{\partial^2}{\partial \eta\partial\zeta}\frac{\partial h_1}{\partial \zeta} - \varepsilon\frac{\eta'}{\mathcal{H}}\frac{\partial}{\partial \eta}\frac{\partial^2 h_1}{\partial \zeta^2} + \mathcal{O}(\varepsilon^2),$$

(27)

$$\frac{\partial}{\partial y} = \frac{1}{\mathcal{H}}\frac{\partial}{\partial \eta} + \varepsilon\frac{1}{\mathcal{H}^2}h_1\frac{\partial}{\partial \eta} + \mathcal{O}(\varepsilon^2),$$

(28)

$$\frac{\partial^2}{\partial y^2} = \frac{1}{\mathcal{H}^2}\frac{\partial^2}{\partial \eta^2} + \varepsilon\frac{1}{\mathcal{H}^3}2h_1\frac{\partial^2}{\partial \eta^2} + \mathcal{O}(\varepsilon^2),$$

(29)

$$\frac{\partial^2}{\partial x\partial y} = \frac{1}{\mathcal{H}}\frac{\partial^2}{\partial \zeta\partial\eta} + \varepsilon\frac{h_1}{\mathcal{H}^2}\frac{\partial^2}{\partial \zeta\partial\eta} - \varepsilon\frac{1}{\mathcal{H}^2}\frac{\partial^2}{\partial \eta^2}\frac{\partial h_1}{\partial \zeta}$$
$$+ \varepsilon\frac{1}{\mathcal{H}^2}\frac{\partial}{\partial \eta}\frac{\partial h_1}{\partial \zeta} + \varepsilon\frac{1}{\mathcal{H}^2}\frac{\partial}{\partial \zeta}\frac{\partial h_1}{\partial \zeta} + \varepsilon\frac{\eta_0}{\mathcal{H}^2}\frac{\partial^2}{\partial \eta^2}\frac{\partial h_1}{\partial \zeta}$$
$$+ \mathcal{O}(\varepsilon^2),$$

(30)

$$\frac{\partial}{\partial t} = \frac{\partial}{\partial \tau} - \varepsilon\frac{\eta'}{\mathcal{H}}\frac{\partial}{\partial \eta}\frac{\partial h_1}{\partial \tau} + \mathcal{O}(\varepsilon^2),$$

(31)

where $\eta' = 1 - \eta_0$. Finally, we combine Eqs. (26)–(31) with Eqs. (13) and (14) to arrive at

$$\frac{\partial \rho_{f1}}{\partial \tau} + \rho_{f0}\frac{\partial u_1^x}{\partial \zeta} + \frac{\rho_{f0}}{\mathcal{H}}\frac{\partial u_1^y}{\partial \eta} = 0,$$

(32)

$$\rho_{f0}\frac{\partial u_1^x}{\partial \tau} = -\frac{\partial p_1}{\partial \zeta} + \frac{1}{\mathcal{H}^2}\mu\frac{\partial^2 u_1^x}{\partial \eta^2} + \mu'\frac{\partial^2 u_1^x}{\partial \zeta^2} + \mu''\frac{1}{\mathcal{H}}\frac{\partial^2 u_1^y}{\partial \zeta\partial\eta},$$

(33)

$$\rho_{f0}\frac{\partial u_1^y}{\partial \tau} = -\frac{1}{\mathcal{H}}\frac{\partial p_1}{\partial \eta} + \mu\frac{\partial^2 u_1^y}{\partial \zeta^2} + \mu'\frac{1}{\mathcal{H}^2}\frac{\partial^2 u_1^y}{\partial \eta^2} + \mu''\frac{1}{\mathcal{H}}\frac{\partial^2 u_1^x}{\partial \zeta\partial\eta},$$

(34)

and Eqs. (21) and (20) to give

$$\frac{\partial \rho_{f2}}{\partial \tau} = -\rho_{f0}\frac{\partial u_2^x}{\partial \zeta} - \frac{\rho_{f0}}{\mathcal{H}}\frac{\partial u_2^y}{\partial \eta} - \mathcal{F}_{\text{avg}}^{\text{mass}},$$

(35)

$$\rho_{f0}\frac{\partial u_2^x}{\partial \tau} = -\frac{\partial p_2}{\partial \zeta} + \frac{\mu}{\mathcal{H}^2}\frac{\partial^2 u_2^x}{\partial \eta^2} + \mu'\frac{\partial^2 u_2^x}{\partial \zeta^2} + \frac{\mu''}{\mathcal{H}}\frac{\partial^2 u_2^y}{\partial \zeta\partial\eta} + \mathcal{F}_{\text{avg}}^{\text{m}-x},$$

(36)

$$\rho_{f0}\frac{\partial u_2^y}{\partial \tau} = -\frac{1}{\mathcal{H}}\frac{\partial p_2}{\partial \eta} + \mu\frac{\partial^2 u_2^y}{\partial \zeta^2} + \frac{\mu'}{\mathcal{H}^2}\frac{\partial^2 u_2^y}{\partial \eta^2} + \frac{\mu''}{\mathcal{H}}\frac{\partial^2 u_2^x}{\partial \zeta\partial\eta}$$
$$+ \mathcal{F}_{\text{avg}}^{\text{m}-y},$$

(37)

where

$$\mathcal{F}_{\text{avg}}^{\text{mass}} = -\rho_{f0}\left(\frac{1}{\mathcal{H}} - \frac{\eta_0}{\mathcal{H}}\right)\left\langle\frac{\partial h_1}{\partial \zeta}\frac{\partial u_1^x}{\partial \eta}\right\rangle + \left\langle u_1^x\frac{\partial \rho_{f1}}{\partial \zeta}\right\rangle$$
$$- \left(\frac{1}{\mathcal{H}} - \frac{\eta_0}{\mathcal{H}}\right)\left\langle\frac{\partial h_1}{\partial \tau}\frac{\partial \rho_{f1}}{\partial \eta}\right\rangle + \frac{1}{\mathcal{H}}\left\langle u_1^y\frac{\partial \rho_{f1}}{\partial \eta}\right\rangle$$
$$+ \rho_{f0}\frac{1}{\mathcal{H}^2}\left\langle h_1\frac{\partial u_1^y}{\partial \eta}\right\rangle + \frac{1}{\mathcal{H}}\left\langle\rho_{f1}\frac{\partial u_1^y}{\partial \eta}\right\rangle + \left\langle\rho_{f1}\frac{\partial u_1^x}{\partial \zeta}\right\rangle,$$

(38)

$$\mathcal{F}_{\text{avg}}^{\text{m}-x} = -\left\langle\rho_1\frac{\partial u_1^x}{\partial \tau}\right\rangle - \frac{\rho_{f0}}{\mathcal{H}}\left\langle u_1^y\frac{\partial u_1^x}{\partial \eta}\right\rangle + \frac{\mu''}{\mathcal{H}^2}\left\langle h_1\frac{\partial^2 u_1^y}{\partial \zeta\partial\eta}\right\rangle$$
$$+ \rho_{f0}\frac{\eta'}{\mathcal{H}}\left\langle\frac{\partial h_1}{\partial \tau}\frac{\partial u_1^x}{\partial \eta}\right\rangle - \rho_{f0}\left\langle u_1^x\frac{\partial u_1^x}{\partial \zeta}\right\rangle$$
$$+ \frac{\eta'}{\mathcal{H}}\left\langle\frac{\partial h_1}{\partial \zeta}\frac{\partial p_1}{\partial \eta}\right\rangle - \mu'\frac{\eta'}{\mathcal{H}}\left\langle\frac{\partial^2 h_1}{\partial \zeta^2}\frac{\partial u_1^x}{\partial \eta}\right\rangle$$
$$+ \frac{1}{\mathcal{H}^2}\mu''\left\langle\frac{\partial h_1}{\partial \zeta}\frac{\partial u_1^y}{\partial \eta}\right\rangle + \frac{2\mu}{\mathcal{H}^3}\left\langle h_1\frac{\partial^2 u_1^x}{\partial \eta^2}\right\rangle$$
$$+ \frac{1}{\mathcal{H}^2}\mu''\left\langle\frac{\partial h_1}{\partial \zeta}\frac{\partial u_1^y}{\partial \zeta}\right\rangle - \mu''\frac{\eta'}{\mathcal{H}^2}\left\langle\frac{\partial h_1}{\partial \zeta}\frac{\partial^2 u_1^y}{\partial \eta^2}\right\rangle$$
$$- 2\mu'\frac{\eta'}{\mathcal{H}}\left\langle\frac{\partial h_1}{\partial \zeta}\frac{\partial^2 u_1^x}{\partial \zeta\partial\eta}\right\rangle,$$

(39)

$$\mathcal{F}_{\text{avg}}^{\text{m}-y} = -\left\langle\rho_1\frac{\partial u_1^y}{\partial \tau}\right\rangle - \frac{\rho_{f0}}{\mathcal{H}}\left\langle u_1^y\frac{\partial u_1^y}{\partial \eta}\right\rangle - \rho_{f0}\left\langle u_1^x\frac{\partial u_1^y}{\partial \zeta}\right\rangle$$
$$+ \rho_{f0}\frac{\eta'}{\mathcal{H}}\left\langle\frac{\partial h_1}{\partial \tau}\frac{\partial u_1^y}{\partial \eta}\right\rangle - 2\mu\frac{\eta'}{\mathcal{H}}\left\langle\frac{\partial h_1}{\partial \zeta}\frac{\partial^2 u_1^y}{\partial \zeta\partial\eta}\right\rangle$$
$$- \frac{1}{\mathcal{H}^2}\left\langle h_1\frac{\partial p_1}{\partial \eta}\right\rangle + \frac{1}{\mathcal{H}^2}\mu''\left\langle\frac{\partial h_1}{\partial \zeta}\frac{\partial u_1^x}{\partial \eta}\right\rangle$$
$$- \frac{\eta'}{\mathcal{H}}\mu\left\langle\frac{\partial^2 h_1}{\partial \zeta^2}\frac{\partial u_1^y}{\partial \eta}\right\rangle - \mu''\frac{\eta'}{\mathcal{H}^2}\left\langle\frac{\partial h_1}{\partial \zeta}\frac{\partial^2 u_1^x}{\partial \eta^2}\right\rangle$$
$$+ \frac{2}{\mathcal{H}^3}\mu'\left\langle h_1\frac{\partial^2 u_1^y}{\partial \eta^2}\right\rangle + \frac{1}{\mathcal{H}^2}\mu''\left\langle\frac{\partial h_1}{\partial \zeta}\frac{\partial u_1^x}{\partial \zeta}\right\rangle$$
$$+ \frac{1}{\mathcal{H}^2}\mu''\left\langle h_1\frac{\partial^2 u_1^x}{\partial \zeta\partial\eta}\right\rangle,$$

(40)

in which $\mu' = \mu_B + (4\mu/3)$; the superscript for the velocity denotes its direction.

B. Boundary conditions

When SAW is coupled with air, a stress-free boundary condition is assumed on the surface of the piezoelectric substrate. As such, the mechanical boundary conditions at each point on the surface of the substrate are $T_{33} = T_{31} = T_{13} = T_{32}$

$=T_{23}=0$ at $x_3=0$ (see Fig. 3). The left, right, and bottom of the substrate are surrounded by a split-field perfectly matched layer (PML) to minimize wave reflection from the boundaries.[58] Within the PML, the wave amplitude decays quadratically with a loss function represented by $\mathcal{D}_i=\mathcal{D}_{\max}[(x_i-x_0)/\delta_{\mathrm{PML}}]^2$,[6,58] where $\mathcal{D}_{\max}$ is an empirical constant, (x_i-x_0) indicates the location of the nodes within the PML layer, and δ_{PML} is the thickness of the PML. To implement the split-field PML for the two-dimensional analysis in x_1- and x_3-space, Eq. (6) is rewritten to separate the derivative into the x_1- and x_3-directions,[59]

$$\left(\frac{\partial}{\partial t}+\mathcal{D}_1\right)v_1^{\parallel}=\frac{1}{\rho_s}\frac{\partial T_1}{\partial x_1},\quad\left(\frac{\partial}{\partial t}+\mathcal{D}_3\right)v_1^{\perp}=\frac{1}{\rho_s}\frac{\partial T_5}{\partial x_3},\quad(41)$$

$$\left(\frac{\partial}{\partial t}+\mathcal{D}_3\right)v_3^{\parallel}=\frac{1}{\rho_s}\frac{\partial T_3}{\partial x_3},\quad\left(\frac{\partial}{\partial t}+\mathcal{D}_3\right)v_3^{\perp}=\frac{1}{\rho_s}\frac{\partial T_5}{\partial x_1},\quad(42)$$

where $v_1=v_1^{\parallel}+v_1^{\perp}$ and $v_3=v_3^{\parallel}+v_3^{\perp}$; the superscripts $\parallel$ and $\perp$ refer to the parallel and perpendicular directions of the associated velocity component, respectively. Abbreviated subscripts are used for the stress field, i.e., $T_1=T_{11}$, $T_3=T_{33}$, and $T_5=T_{13}=T_{31}$. To generate the SAW, a sinusoidal electric potential,

$$\phi=\phi_{\mathrm{p-p}}\sin(2\pi x_i/\lambda_{\mathrm{SAW}})\sin(\omega t),\quad(43)$$

where $\phi_{\mathrm{p-p}}$ is the peak-to-peak voltage, is applied on the surface of the piezoelectric substrate.

At the air-liquid interface, $y=0$, we impose the following tangential and normal stress conditions, respectively, given by

$$2\left(\frac{\partial u^x}{\partial x}-\frac{\partial u^y}{\partial y}\right)\frac{\partial h}{\partial x}+\left(\frac{\partial u^y}{\partial x}+\frac{\partial u^x}{\partial y}\right)\left[1-\left(\frac{\partial h}{\partial x}\right)^2\right]=0,\quad(44)$$

$$p=\gamma_c\kappa_c+\mu'''\boldsymbol{\nabla}\cdot\mathbf{u}$$
$$+\frac{2\mu\left[\frac{\partial u^x}{\partial x}\left(\frac{\partial h}{\partial x}\right)^2+\left(\frac{\partial u^y}{\partial x}+\frac{\partial u^x}{\partial y}\right)\frac{\partial h}{\partial x}+\frac{\partial u^y}{\partial y}\right]}{\left(\frac{\partial h}{\partial x}\right)^2+1},\quad(45)$$

where γ_c denotes surface tension and $\mu'''=\mu_B-(2\mu/3)$. On the other hand, the surface curvature κ_c is given by

$$\kappa_c=\frac{\partial^2 h}{\partial x^2}\left[1+\left(\frac{\partial h}{\partial x}\right)^2\right]^{-3/2}.\quad(46)$$

In addition to the above, the kinematic boundary condition is also imposed,

$$\frac{\partial h}{\partial t}+u^x\frac{\partial h}{\partial x}=u^y.\quad(47)$$

By substituting Eqs. (10), (11), (24), and (26)–(31) into Eqs. (44), (45), and (47), we obtain the boundary conditions at $y=0$ for the first-order flow field by selecting terms of order $\mathcal{O}(\varepsilon)$,

$$\frac{\partial u_1^y}{\partial\zeta}+\frac{1}{\mathcal{H}}\frac{\partial u_1^x}{\partial\eta}=0,\quad(48)$$

$$p_1=\mu'''\left[\frac{\partial u_1^x}{\partial\zeta}+\frac{1}{\mathcal{H}}\frac{\partial u_1^y}{\partial\eta}\right]+\frac{2\mu}{\mathcal{H}}\frac{\partial u_1^y}{\partial\eta}+\gamma_c\frac{\partial^2 h_1}{\partial\zeta^2},\quad(49)$$

$$\frac{\partial h_1}{\partial\tau}=u_1^y,\quad(50)$$

and, the boundary conditions at $y=0$ for the second-order flow field by selecting terms of order $\mathcal{O}(\varepsilon^2)$,

$$\frac{\partial u_2^y}{\partial\zeta}=-\frac{1}{\mathcal{H}}\frac{\partial u_2^x}{\partial\eta}-2\left\langle\frac{\partial h_1}{\partial\zeta}\frac{\partial u_1^x}{\partial\zeta}\right\rangle-\frac{1}{\mathcal{H}^2}\left\langle h_1\frac{\partial u_1^x}{\partial\eta}\right\rangle$$
$$+\frac{3}{\mathcal{H}}\left\langle\frac{\partial h_1}{\partial\zeta}\frac{\partial u_1^y}{\partial\eta}\right\rangle,\quad(51)$$

$$p_2=\gamma_c\frac{\partial^2 h_2}{\partial\zeta^2}+\frac{2\mu}{\mathcal{H}}\frac{\partial u_2^y}{\partial\eta}+\mu'''\left[\frac{\partial u_2^x}{\partial\zeta}+\frac{1}{\mathcal{H}}\frac{\partial u_2^y}{\partial\eta}\right]$$
$$+\frac{2\mu}{\mathcal{H}}\left\langle\frac{\partial h_1}{\partial\zeta}\frac{\partial u_1^x}{\partial\eta}\right\rangle+\frac{2\mu}{\mathcal{H}^2}\left\langle h_1\frac{\partial u_1^y}{\partial\eta}\right\rangle$$
$$-\mu'''\frac{1}{\mathcal{H}}\left\langle\frac{\partial h_1}{\partial\zeta}\frac{\partial u_1^x}{\partial\eta}\right\rangle+\frac{1}{\mathcal{H}^2}\mu'''\left\langle h_1\frac{\partial u_1^y}{\partial\eta}\right\rangle$$
$$+2\mu\left\langle\frac{\partial h_1}{\partial\zeta}\frac{\partial u_1^y}{\partial\zeta}\right\rangle,\quad(52)$$

$$\frac{\partial h_2}{\partial\tau}=u_2^y-\left\langle u_1^x\frac{\partial h_1}{\partial\zeta}\right\rangle.\quad(53)$$

A no-slip boundary condition is imposed on the left and right walls $x=(0,\mathcal{L})$: $u_1^y=u_1^x=0$ and $u_2^y=u_2^x=0$. In addition, the no-slip condition implies the height fluctuation should also be zero on the walls: $h_1=0$ and $h_2=0$ at $x=(0,\mathcal{L})$. At the solid-fluid interface $y=\mathcal{H}$ and between $x=\mathcal{L}_1$ and $\mathcal{L}_4$ (see Fig. 3), the first-order velocity and pressure of the fluid are coupled with the solid substrate through continuity of velocity, $u_1^x=v_1$, $u_1^y=v_3$, and stress conservation, $\int_{x=\mathcal{L}_1}^{x=\mathcal{L}_4}\sigma_{33}=\int_{x=\mathcal{L}_1}^{x=\mathcal{L}_4}T_{33}$ and $\int_{x=\mathcal{L}_1}^{x=\mathcal{L}_4}\sigma_{13}=\int_{x=\mathcal{L}_1}^{x=\mathcal{L}_4}T_{13}$. As for the second-order field, we employ the velocity boundary condition,[50]

$$\mathbf{u}_2|_{y=\mathcal{H}}=-\frac{1}{2}\boldsymbol{\nabla}\times\langle\xi_1^{\mathrm{f}}\times\mathbf{u}_1\rangle,\quad(54)$$

where ξ_1^{f} is the displacement of the fluid element. This condition arises as a result of the elliptical motion of the solid substrate (acoustic radiator) as the SAW propagates along the substrate surface. In addition, the left and right ends in the fluid domain of the first-order field are surrounded by the split-field PML to minimize wave reflections. This implementation is similar to that for the solid. Equation (32) can therefore be rewritten as

$$\left(\frac{\partial}{\partial t}+\mathcal{D}_1\right)\rho_1^{\parallel}=-\rho_{\mathrm{f0}}\frac{\partial u_1^x}{\partial\xi},\quad\left(\frac{\partial}{\partial t}+\mathcal{D}_3\right)\rho_1^{\perp}=\frac{\rho_{\mathrm{f0}}}{\mathcal{H}}\frac{\partial u_1^y}{\partial\eta},\quad(55)$$

where $\rho_1=\rho_1^{\parallel}+\rho_1^{\perp}$.

C. Numerical method

The necessary equations to be solved for the piezoelectric solid involve the time-domain constitutive piezoelectric equations, i.e., Eqs. (4) and (5), Newton's second law of motion, i.e., Eq. (6), and the PML boundary condition, i.e., Eqs. (41) and (42). In addition, Eq. (43) is required to generate the electric field in the substrate. For the acoustic field in the fluid, the appropriate equations are continuity, i.e., Eq. (32), momentum conservation equations (33) and (34), and the equation of state, i.e., Eq. (15). On the free surface of the fluid, the equations for the normal stress jump, i.e., Eq. (48), tangential stress continuity, i.e., Eq. (49), and the kinematic boundary condition, i.e., Eq. (50), are solved simultaneously using the finite-difference time-domain method.[55,60] The equations of motion for the solid are discretized using a second-order centered difference scheme and the variables are distributed on a staggered-spatiotemporal-grid system, where stress and electric fields are located at the same nodes and velocities occupy the others. However, due to the difficulties in computing the fluid variables at the free surface on a spatially staggered grid, variables for the fluid are allocated on a spatially collocated but temporally staggered grid system. These equations are also discretized using a second-order centered difference scheme. The stress and electric fields of the solid, and the pressure and density fields of the fluid, are allocated at the same time frame at $(n/2)\delta t$, where n is a positive integer and δt is the time step. Similarly, the velocity fields for the solid and fluid are allocated at the same time frame at $n\delta t$. To ensure stability of the numerics, the largest Courant number of the solid or fluid domain $C = c\delta t/\delta x$,[61] where c is the phase velocity of the wave and δx is the grid spacing, is selected (approximately 0.02) to determine the maximum allowable time step δt. Since we select identical δt for both the solid and fluid, the calculations can be carried out synchronously. In other words, the equations for solving the solid variables at time $(n/2)\delta t$ are solved in parallel with the equations for solving the fluid variables at time $(n/2)\delta t$.

In each time step, the terms in the $\langle \rangle$ brackets are computed and summed over one sinusoidal cycle (i.e., to numerically approximate the time integration of each term in the brackets). To complete the time averaging, these terms are then divided by the number of steps to complete the cycle and subsequently substituted back into Eqs. (38)–(40) and Eqs. (51)–(53). After one cycle is completed, we temporary halt the computation of the acoustic fields in the solid and fluid, and proceed to calculate the acoustic streaming field. The streaming field involves solving the equations governing continuity, i.e., Eq. (35), momentum conservation, i.e., Eqs. (36) and (37), and the equation of state, i.e., Eq. (19). In addition, the tangential stress balance at the free surface, i.e., Eq. (51), the normal stress jump at the free surface, i.e., Eq. (52), the kinematic boundary condition at the free surface, i.e., Eq. (53), and the velocity boundary condition at the solid-fluid interface, i.e., Eq. (54), are also required. The numerical scheme used to solve the second-order field is identical to the method used to solve the first-order field. In our model, the dimension of the solid domain is 4.8 mm long

(x_1-axis) and 1.6 mm deep (x_3-axis), and the dimension of the fluid domain is 2 mm long (x-axis) and 0.4 mm deep (y-axis). The spacing between nodes in the solid and fluid domain are 4 and 2 μm, respectively. However, in the fluid domain and at regions adjacent to the solid substrate, a denser grid is required to capture the boundary layer thickness[49] $\delta_v = (\mu/2\pi\rho_f f)^{1/2} \sim 100$ nm generated by 20 MHz acoustic waves. Therefore, the node spacing along the y-direction in this region has been reduced to 20 nm in order to provide approximately five computational points within the boundary layer.

D. Results

Figure 4 shows the results from a discrete Fourier transform (DFT) of the free surface displacement at point A (Fig. 3) from a time to frequency domain, i.e., $h(t) \to \hat{h}(\omega)$, where $h(t) = h_1(t) + \varepsilon h_2(t)$. The $\hat{h}$ spectra therefore constitute quadratic terms of order $\mathcal{O}(\varepsilon)$ smaller than their linear counterparts, representing weak nonlinearities. With the presence of nonlinear terms in the equations, the solution may constitute harmonic waves[62] with frequencies 0, 2ω, 3ω, 4ω,... The number of points for each data set is 53 900 and the sampling rate is 523 MHz. Therefore, the upper bound on the highest frequency the recorded data can capture is approximately 261 MHz (Nyquist frequency) and the lower bound is approximately 10 kHz. The lowest frequency is limited by the total sampling time, approximately 103 μs. We examine the effects of varying the surface displacement magnitude of the substrate, $|\xi| \approx 0.3$, 1.2, and 2.5 nm, in Figs. 4(a)(i), 4(a)(ii), 4(b)(i), 4(b)(ii), and 4(c)(i), 4(c)(ii), respectively, and of varying the initial film thickness, $\mathcal{H} = 400$ and 600 μm, in Figs. 4(b)(i), 4(b)(ii) and 4(d)(i), 4(d)(ii), respectively.

The results in Fig. 4 clearly show that the resonant frequency f_0 of the free surface is 20 MHz, identical to the applied SAW frequency and consistent with the previously reported findings of Li *et al.*[63] No distinct subharmonic capillary frequency at $f_c = f_0/2 \approx 10$ MHz can be identified, which is in agreement with the Qi *et al.*'s experimental findings,[16] and quite contrary to the original Faraday experiment[22] and the classical theories that have since followed.[23–25] Within the frequency band of 1–10 MHz, no specific pattern of the frequency spectra can be identified [Figs. 4(a)(i), 4(b)(i), 4(c)(i), and 4(d)(i)]. In addition, the broadband low-frequency vibrations ($f_c < 1$ MHz $\ll f_0$), first observed by Qi *et al.*,[16] are absent in our numerical results. This is anticipated as the excitation of the low-frequency vibration is associated with the high-amplitude SAW and fast streaming regime, i.e., $\text{Re}_A > 1$, where Re_A is the acoustic Reynolds number, given by

$$\text{Re}_A = \frac{\rho_f u_1 \lambda_f}{2\pi\mu'}. \tag{56}$$

The present model, which is based on successive approximations, is, however, limited to the low-amplitude SAW and slow streaming regime, i.e., $\text{Re}_A < 1$, since $\varepsilon h_2 \ll h_1$ is a necessary requirement of the regular perturbation expansion. We
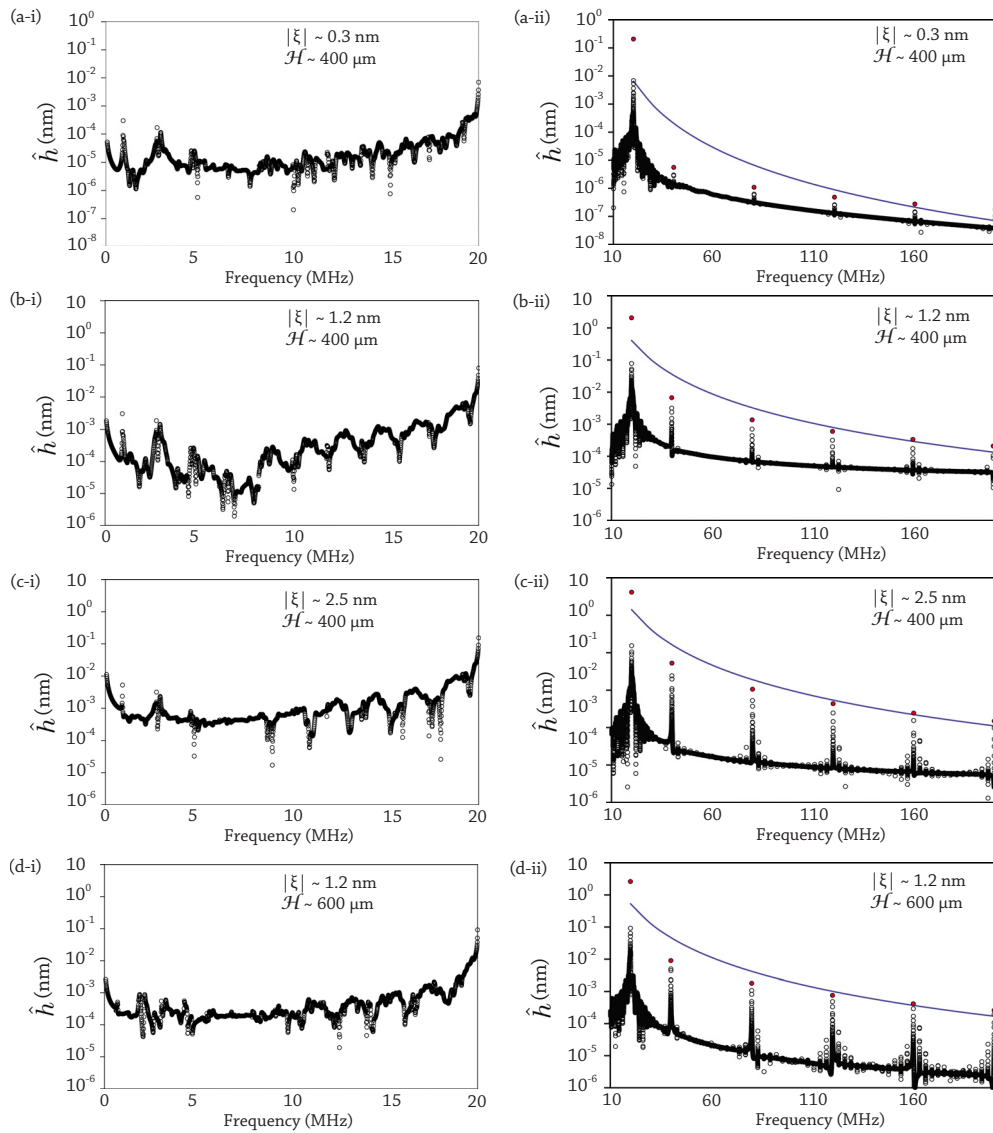
FIG. 4. (Color online) Numerical results from the DFT of h at point A (see Fig. 3). Three substrate displacement magnitudes $|\xi|$—[(a)(i) and (a)(ii)] 0.3 nm, [(b)(i) and (b)(ii) and (d)(i) and (d)(ii)] 1.2 nm, and, [(b)(i) and (b)(ii)] 2.5 nm—and two different initial thicknesses for the liquid film—[(a)(i) and (a)(ii), (b)(i) and (b)(ii), and (c)(i) and (c)(ii)] 400 μm and [(d)(i) and (d)(ii)] 600 μm—are selected for the analysis. In this figure, the frequency spectra for each substrate displacement magnitude $|\xi|$ are separated for clarity. Six resonant frequencies are identifiable (marked by the solid-dots). The solid line represents a regression fit of the data, which are based on the power law $\hat{h}(f) = Cf^{-q}$ with the regression coefficients q of 0.79, 0.9, 0.94, and 0.9 for (a)(ii), (b)(ii), (c)(ii), and (d)(i), respectively. The acoustic Reynolds number is approximately $\mathrm{Re}_A \approx 0.15$ for $|\xi| \approx 0.3$ nm, $\mathrm{Re}_A \approx 0.5$ for $|\xi| \approx 1.2$ nm, and $\mathrm{Re}_A \approx 1$ for $|\xi| \approx 2.5$ nm.

note here that the phrase "successive approximations" is often used in the acoustic streaming literature instead of perturbation expansion to describe the analysis technique.

Nonetheless, the results do show the existence of weak superharmonic resonant frequencies at $f_1^+ \approx 40$ MHz $\sim 2f_0$, $f_2^+ \approx 80$ MHz $\sim 4f_0$, $f_3^+ \approx 120$ MHz $\sim 6f_0$, $f_4^+ \approx 160$ MHz $\sim 8f_0$, and $f_5^+ \approx 200$ MHz $\sim 10f_0$ (see Fig. 4). The free surface displacements $\hat{h}$ at these superharmonic frequencies are at least two orders of magnitude smaller than the resonant frequency f_0. The value of $|h|$ at f_{1-6}^+ decreases, following a power law in the frequency domain, as shown by the solid line in Fig. 4. A power law relationship between the peak amplitude at each resonance and the frequency may be expressed by $\hat{h}(f) = Cf^{-q}$, where C and q are constants. The estimated exponent q for the curves in Figs. 4(a)–4(d) is ap-

proximately 4.9, 3.5, 3.1, and 3.5, respectively. For the power law analysis, an increase in q (larger $\hat{h} - f$ slope) is associated with a lower content of harmonics at higher frequencies, resulting in a purer monofrequency sinusoidal response at the excitation frequency f_0, whereas a smaller q (smaller $\hat{h} - f$ slope) represents higher amplitudes of the harmonics and, hence, a weaker monofrequency sinusoidal response. Increasing the SAW amplitude can increase the magnitude of $\hat{h}$ at the superharmonic frequencies, which then results in smaller q. As the height of the liquid film increases, more sideband frequencies appear, showing an increase of the content of harmonics at higher frequencies. Therefore, within $\mathrm{Re}_A < 1$, the shape of the deformed surface becomes slightly less sinusoidal by increasing the magnitude of the
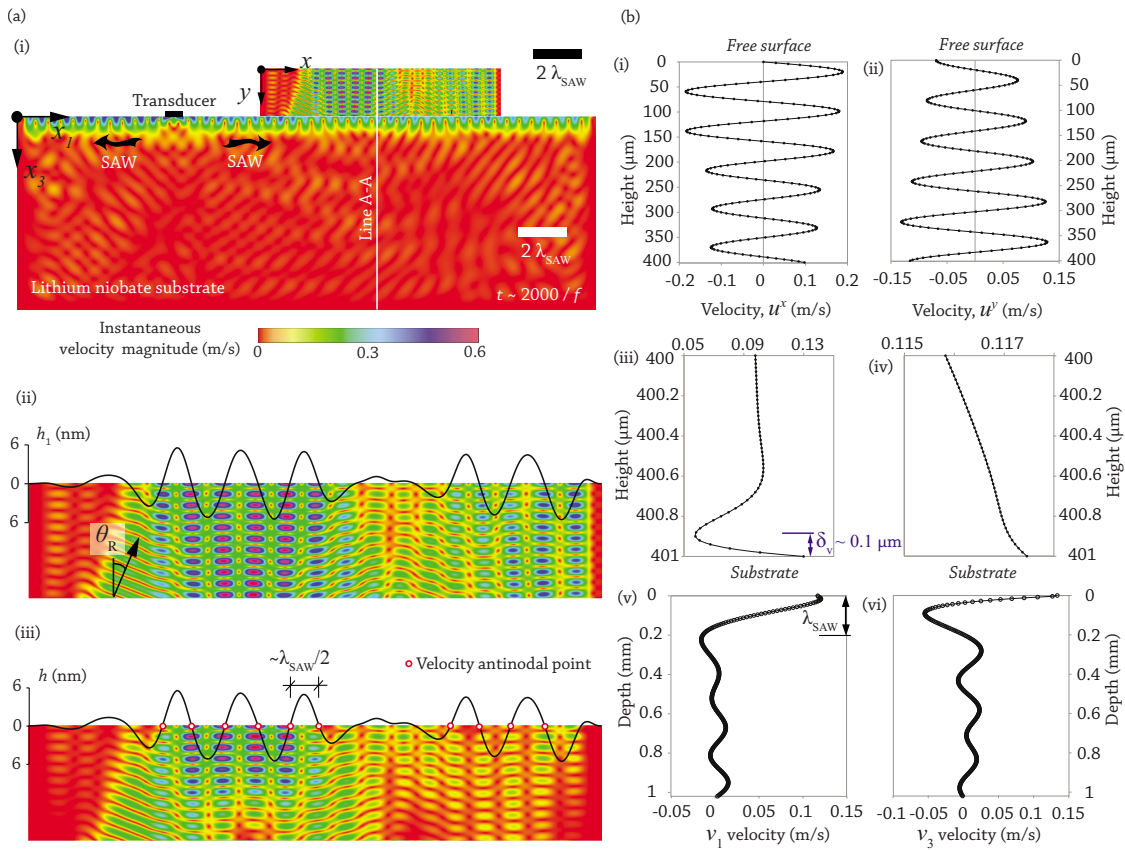
FIG. 5. (Color online) (a)(i) Computed acoustic velocity field (color density plot) in the solid and in the fluid after $t=2000f_{SAW}^{-1}$, i.e., after 2000 sinusoidal cycles each of period f_{SAW}^{-1} seconds. At the solid-fluid interface, the transmission of acoustic waves into the fluid begins at a distance away from the left wall, i.e., interactions between solid and fluid only within $\mathcal{L}_1-\mathcal{L}_4$ as shown in Fig. 3. (a)(ii) Enlarged view of the fluid domain showing the instantaneous acoustic velocity field $\mathbf{u}_1$ and the computed instantaneous displacement h_1. The Rayleigh angle θ_R is approximately 23°, which is very close to the theoretical prediction of $\theta_R \equiv \sin^{-1}(c/c_s) \approx 22°$, where $c=1485$ m/s is the sound speed in the fluid and $c_s=3965$ m/s is the sound speed in the substrate. (a)(iii) Magnitude of the velocity field $\mathbf{u}$ in the fluid and the instantaneous displacement of the free surface h, showing the formation of capillary waves on the liquid/gas interface. The instantaneous displacement of the free surface has been exaggerated for clarity. The profiles of h_1 and h are almost identical, suggesting that the contribution of εh_2 is negligible. However, adjacent to the free surface, the contribution of $\varepsilon \mathbf{u}_2$ augments the velocity of the standing wave and hence facilitates the collection of particles in this region, consistent with the results reported by Li *et al.* (Ref. 63). The distance between two adjacent acoustic velocity antinodal points is approximately 114 μm $\approx \lambda_{SAW}/2$. The velocity profiles along line A-A are shown in (b): [(i) and (ii)] instantaneous u^x and u^y velocity amplitude in the bulk of the fluid, [(iii) and (iv)] instantaneous u^x and u^y velocity amplitude at the region adjacent to the substrate surface, and [(v) and (vi)] instantaneous v_1 and v_3 velocity amplitudes in the substrate.

SAW and/or the height of the liquid film. Also, as discussed in Sec. I, the presence of superharmonics and period-halving behavior is always associated with a likewise subharmonic, period-doubling sequence. We, therefore, expect the subharmonic frequencies, from f_0 to $f_0/10$, to be present although they are not discernible in the results presented in Figs. 4(a)(i), 4(b)(i), 4(c)(i), and 4(d)(i); this is due to limitations of the model, which are highlighted below.

Figure 5(a)(i) shows the computed velocity field of the solid and the fluid film of height $\mathcal{H} \approx 400$ μm after $t = 2000f^{-1}$ s, as a consequence of 20 MHz SAW excitation. The displacement magnitude of the substrate is $|\xi| \sim 1.2$ nm excited by a 10 V_{p-p} potential applied to the substrate. Figure 5(a)(ii) shows details of the decomposed instantaneous acoustic velocity field $\mathbf{u}_1$, and Fig. 5(a)(iii) shows the total fluid velocity field $\mathbf{u}$. Within the fluid domain, the amplitude of the acoustic particle velocity $\mathbf{u}_1 \sim \mathcal{O}(10^{-1})$ m/s and the amplitude of the second order velocity $\varepsilon \mathbf{u}_2 \sim \mathcal{O}(10^{-6})$ m/s, indicating that the flow is in the

low-amplitude SAW regime ($Re_A < 1$). The numerical results, therefore, remain valid after 2000 cycles since the condition of $\mathbf{u}_1 \gg \varepsilon \mathbf{u}_2$ is still satisfied.

The velocity profiles along the line A-A in Fig. 5(a)(i) are shown in Fig. 5(b). On the free surface, the wavelength along the x-direction is approximately $\lambda_c \approx 228$ μm and, within the bulk of the fluid, the wavelength along the y-direction is approximately 80 μm [see Figs. 5(b)(i) and 5(b)(ii)]. By comparing the wavelength in the y-direction to the acoustic wavelength in the fluid, $\lambda_f \sim 75$ μm for a 20 MHz acoustic wave, the results suggest that the compressional acoustic waves are propagating in the fluid predominantly along the y-direction. The waves arriving at the air-liquid interface are then reflected back into the liquid due to the acoustic impedance mismatch of the air ($\sim 10^3$ kg m^{-2} s) and water ($\sim 10^6$ kg m^{-2} s). Similarly, waves arriving at the solid-fluid interface are partially reflected into the fluid. The superposition of these reflected and incident waves forms strong acoustic standing waves in the
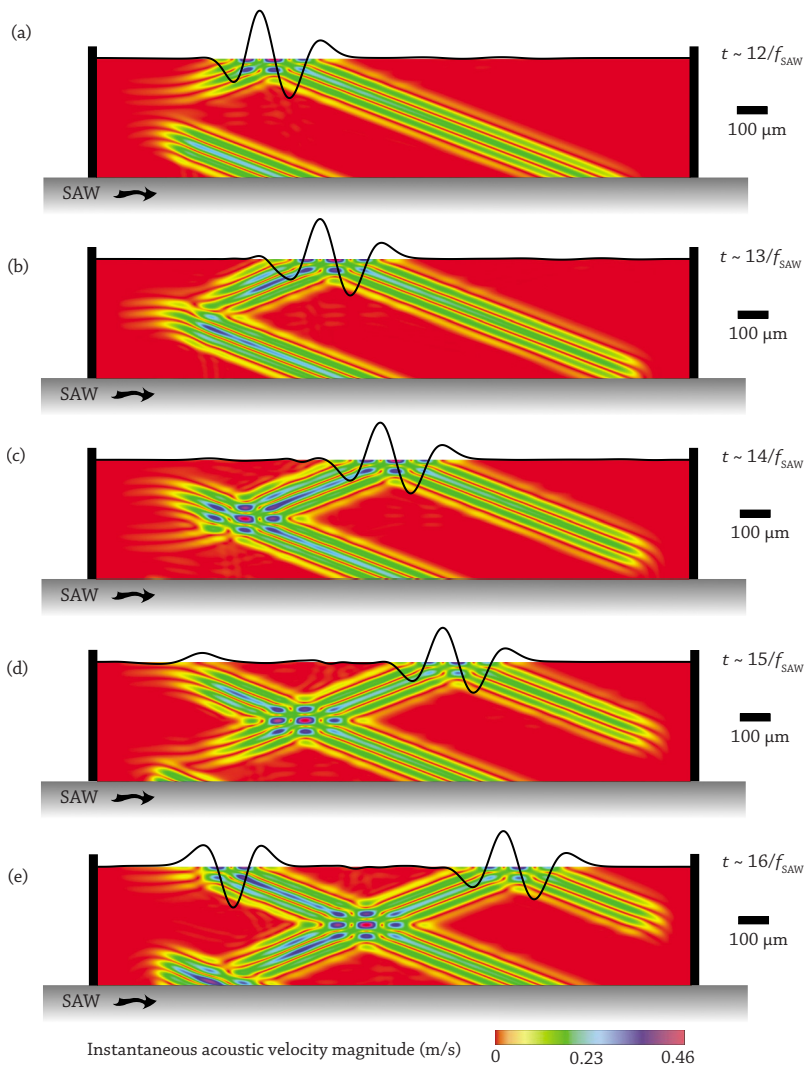
FIG. 6. (Color online) Numerical results showing the propagation/reflection of acoustic waves into a flat liquid film ($\mathcal{H} \sim \mathcal{L}$) at $t=$ (a) $12 f_{SAW}^{-1}$, (b) $13 f_{SAW}^{-1}$, (c) $14 f_{SAW}^{-1}$, (d) $15 f_{SAW}^{-1}$, and (e) $16 f_{SAW}^{-1}$ s, under a 20 MHz pulse mode excitation (one cycle on and four cycles off of a sinusoidal signal). The sequential images show the formation of strong acoustic standing waves in the y-direction and a moving grid-structure within the liquid film. The instantaneous displacement h_1 of the free surface has been exaggerated for clarity.

y-direction; the mechanism is similar to *Bragg resonance* resulting from the interaction of the free surface waves on water and the (stationary) undulating seabed as observed by Heathershaw.[64] In order to illustrate the interference of acoustic waves more clearly, we use a 20 MHz pulse mode excitation (one cycle on and four cycles off of a sinusoidal signal) and extract only the first-order results at $t=12 f_{SAW}^{-1}$, $13 f_{SAW}^{-1}$, $14 f_{SAW}^{-1}$, $15 f_{SAW}^{-1}$, and $16 f_{SAW}^{-1}$ seconds, as shown in Figs. 6(a)–6(e), respectively.

Curiously, the wavelength in the x-direction λ_c more closely matches the SAW wavelength, $\lambda_{SAW} \sim 200$ μm. This indicates that the compressional wave that propagates in the y-direction is strongly coupled with the SAW on the substrate. This results in a *phase-locking* phenomenon[65] in which the phase of the u_1^y velocity at the air-liquid interface is in-phase with the v_3 velocity at the solid-fluid interface. The process is more clearly illustrated in Fig. 6, showing the superposed acoustic waves forming a moving "grid-structure," which then appears to assist the phase-locking mechanism. Moreover, the result obtained for the $\mathcal{H} \approx 600$ μm film (not shown) reveals that λ_c is increased further to approximately 270 μm, suggesting the λ_c is a function of the film height; that is, λ_c increases with increasing

film height. We attribute this to be caused by the dispersion of acoustic waves and the weakening of the phase-locking mechanism, whereby the effect should be strongest for $\mathcal{H} \leq \lambda_{SAW}$. Next to the substrate surface, a thin viscous boundary layer of thickness $\delta_v \sim 0.1$ μm is generated, as shown in Figs. 5(b)(iii) and 5(b)(iv). The velocities of the piezoelectric substrate along line A-A are also shown in Figs. 5(b)(v) and 5(b)(vi). The displacement of the substrate as the SAW propagates across it is mostly confined within a SAW wavelength from the free surface, i.e., from $x_3=0$ to $x_3=\lambda_{SAW}$.

At the free surface of the fluid, acoustic velocity antinodal points are formed as shown in Fig. 5(a)(iii). We note here that from linear acoustic theory, a displacement nodal point is equivalent to an antinode in the velocity due to the 90° phase difference between the displacement and velocity field. The instantaneous displacement of the free surface is therefore at an equilibrium state ($h=0$) at displacement nodal points or at velocity antinodal points [Fig. 5(a)(iii)]. The formation of a standing wave on the free surface here is consistent with Li *et al.*'s experimental results,[63] wherein the clustering of nanoparticles on the free surface of a slender droplet ($\mathcal{L} \gg \mathcal{H}$) along lines specified by the displacement

antinodal locations is reported. The interval between two adjacent particle cluster lines is approximately 100 μm $\approx \lambda_{SAW}/2$, which compares favorably with the fluid velocity field in Fig. 5(a)(iii).

Further evidence for the formation of standing waves is obtained from Alvarez *et al.*'s experimental analysis[20] in which they report the spreading of a polymer drop atop a SAW device into a thin film ($\mathcal{L} \gg \mathcal{H}$). Breakup occurs across the entire free surface due to the depletion and rupture of the film at the acoustic velocity antinodal positions. Due to a transverse instability across a two-dimensional free surface, the velocity antinodal points form a hexagonal closed-packed lattice[66] and with a longitudinal pitch spacing equivalent to $\lambda_{SAW}/2$.[20] As a consequence, the polymer spots appear in an offset close-packed pattern. We note here that the distance of $\lambda_{SAW}/2$ on the free surface and the phase-locking phenomenon requires $\mathcal{L} \gg \mathcal{H}$; that is, the free surface is relatively flat and parallel to the substrate, and with a small film height ($\mathcal{H} \sim \lambda_{SAW}$).

In summary, the numerical model above, based on successive approximations, is not capable of capturing the broadband low-frequency vibration ($f_c \ll f_0$) driven by high-amplitude SAW excitation ($\mathrm{Re}_A > 1$), observed experimentally.[16] The displacement amplitude of the free surface in the experiments is far larger than the substrate displacement, i.e., $h \gg \xi$. However, the numerical results (Fig. 4) show the computed values of h and ξ to be of the same order of magnitude, $h \sim \xi$. This is primarily due to the criteria of the method of successive approximations in which $h_1 \gg \varepsilon h_2$ and $h_1 \sim \xi$ as a result of the linearization of the first-order acoustic field. This can be more clearly demonstrated by Eq. (50) in which the linearized kinematic equation shows that the time-derivative of h_1 varies linearly with u_1^y; since the acoustic field in the fluid is linear, we expect $|\mathbf{v}| \sim |\mathbf{u}_1|$ for acoustic waves in a bounded medium with negligible acoustic absorption coefficient α. We also note that the $h \sim \xi$ restriction causes the suppression of apparent deformations, which requires $h \sim \mathcal{H}$ [see Figs. 1 and 10(a)(iv)]. The successive approximation method also limits the second-order field to slow streaming and hence is not capable of capturing the fast-moving streaming. Furthermore, the two-dimensional model only allows a limited interaction of wave vectors (of capillary waves) as a consequence of the reduced dimension of the free surface; the free surface is modeled as a single-line in a two-dimensional model. The importance of using more than one-dimension for the free surface is clearly demonstrated in the experiments in which capillary wave patterns are formed—the transition between patterns on a two-dimensional free surface is associated with the interaction of wave vectors, thereby generating subharmonic/superharmonic waves.[67,68] The interaction between wave vectors could also result in the cascade of subharmonic frequencies and give rise to the broadband low-frequency phenomenon observed. Therefore, the high-amplitude vibration of the free surface (with nonrestricted degree of freedoms) in the low-frequency band will be analyzed using experimental techniques in Sec. III.
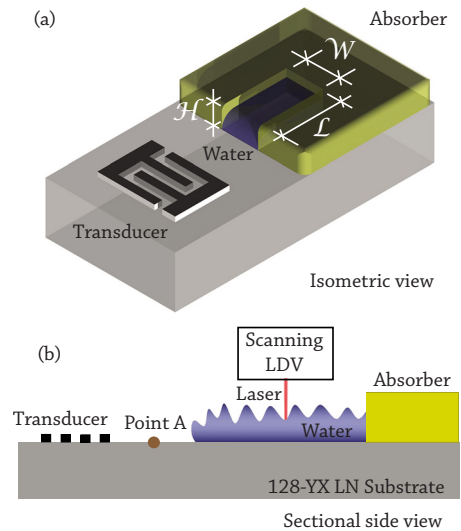

FIG. 7. (Color online) Schematic illustrating the experimental setup employed to measure the capillary wave vibration. (a) To minimize wave reflections, the water was contained within an absorber except on the side from which the SAW approached. (b) A sectional side view shows the locations where the vertical displacement was measured using the scanning LDV.

III. EXPERIMENTS

A. Experimental setup

The experimental setup is shown in Fig. 7. The interdigital transducer (IDT) was fabricated on 500 μm thick, 127.68°-rotated Y-cut X-propagating single-crystal lithium niobate (128-YX-LN) substrates (Roditi Ltd., London, UK), using a standard UV photolithography process. We used dual-layer metallization for the IDT; a titanium layer of thickness of 4 nm is first deposited followed by an aluminum layer of thickness of 250 nm. The design was based on a conventional bidirectional IDT scheme[69,70] and consists of 30 electrode finger pairs, each of width $\lambda_{SAW}/4 \approx 200$ μm, to generate a 20 MHz SAW.

To contain the fluid, a rectangular area of approximately 10 mm in length $\mathcal{L}$, 5 mm in width $\mathcal{W}$, and 5 mm in height $\mathcal{H}$, was placed on the substrate using a damping material (α-gel, Geltec Ltd., Yokohama, Japan), as shown in Fig. 7(a). This material absorbs the SAW energy, thus minimizing wave reflection. The liquid was dispensed until the thickness of the film reached $\sim$1 mm. A scanning laser Doppler vibrometer (LDV) (MSA-400, Polytec PI, Waldbrunn, Germany) was used to record the vertical (perpendicular to the substrate) displacement of the fluid free surface at a sampling rate of 52 MHz; 2^{20} data points were recorded for each measurement.[71] The Nyquist frequency is 26 MHz (half of the sampling frequency), which is the highest frequency the recorded data can accurately represent. The lowest frequency is determined by the total sampling time, approximately 0.02 s. The lowest frequency is therefore 50 Hz. Thus, frequency data outside the band from 50 Hz to 26 MHz are discarded. The recorded time-domain data were subsequently
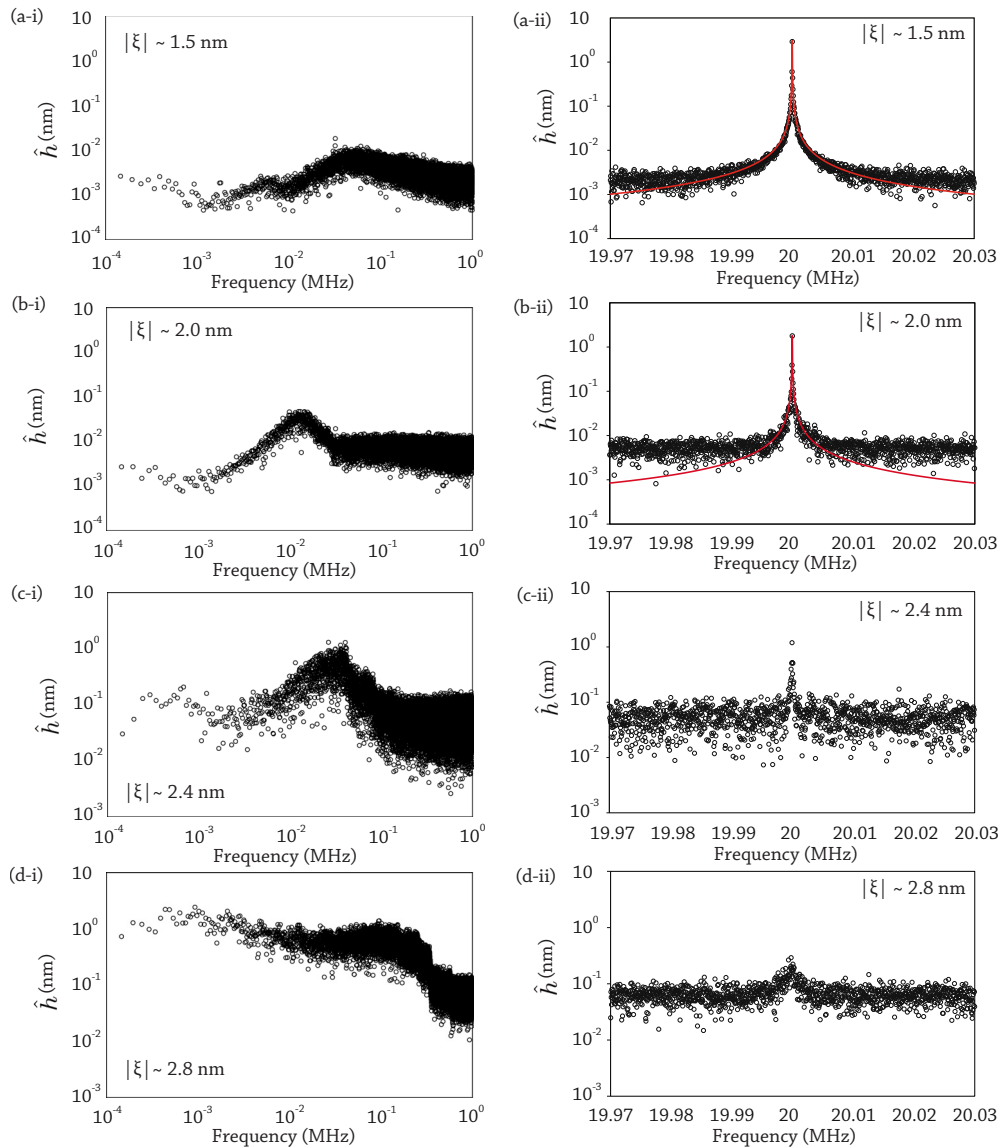
FIG. 8. (Color online) Capillary wave frequency spectra over a range of vertical substrate displacement magnitudes measured using the LDV at low kilohertz order frequencies—(a)(i) $|\xi| \approx 1.5$ nm, (b)(i) 2.0 nm, (c)(i) 2.4 nm, and, (d)(i) 2.8 nm—and high megahertz order frequencies—(a)(ii) $|\xi| \approx 1.5$ nm and $\hat{h}_{\text{peak}} \approx 2.9$ nm, (b)(ii) $|\xi| \approx 2.0$ nm and $\hat{h}_{\text{peak}} \approx 1.8$ nm, (c)(ii) $|\xi| \approx 2.4$ nm and $\hat{h}_{\text{peak}} \approx 1.2$ nm, and (d)(ii) $|\xi| \approx 2.8$ nm and $\hat{h}_{\text{peak}} \approx 0.3$ nm—when driven by a 20 MHz SAW. In this figure, the frequency spectra for each substrate displacement magnitude $|\xi|$ are separated for clarity. The frequency spectra between 0.1 kHz and 1 MHz show that the free surface vibration spectra broadens considerably as the SAW magnitude increases from $|\xi| \approx$ (a)(i) 1.5 to (d)(i) 2.8 nm. On the other hand, the high frequency measurements show a single peak at 20 MHz, which is the excitation frequency, and the peak becomes increasingly weak as the SAW magnitude increases from $|\xi| \approx$ (a)(i)1.5 nm to (d)(ii) 2.8 nm. The solid line is the Lorentzian function used to fit to the data.

transformed into the frequency domain using a fast Fourier transform. For all measurements, water was mixed with black food coloring (Queen Fine Foods Pty. Ltd., Queensland, Australia) to enhance the reflection of the laser beam from the free surface and to reduce the reflected light from the substrate to ensure that the time-domain displacement data of the capillary waves is independent of the time-domain displacement data of the vibrating substrate. At each input power, the vertical displacement amplitude of the substrate at point A [see Fig. 7(b)] was measured. Four different magnitudes were selected—1.5, 2, 2.4, and 2.8 nm—for the study of the transition from different flow regimes. We note here that no SAW atomization occurred for this range of displacement magnitudes.

B. Results and discussion

Figure 8 shows the frequency spectrum of the free surface vibration. Only a single peak at 20 MHz is observed for low magnitude SAW excitation, i.e., $|\xi| \sim 1.5$ and 2.0 nm. As shown by the solid line, the resonances represented by the data in Figs. 8(a)(ii) and 8(b)(ii) are Lorentzian and may be expressed by $L(\omega) = \pi^{-1}\Gamma / [(\omega - \omega_0)^2 + \Gamma^2]$, where Γ specifies the width and ω_0 is the central frequency, indicating the phenomena at the current excitation amplitude is linear. By increasing the SAW magnitude to $|\xi| \sim 2.4$ and 2.8 nm, the amplitude of the 20 MHz vibration peak of the free surface decreases significantly, as shown in Figs. 8(c)(ii) and 8(d)(ii), respectively, and the Lorentzian function no longer fits the data. This suggests that the system's response begins to de-
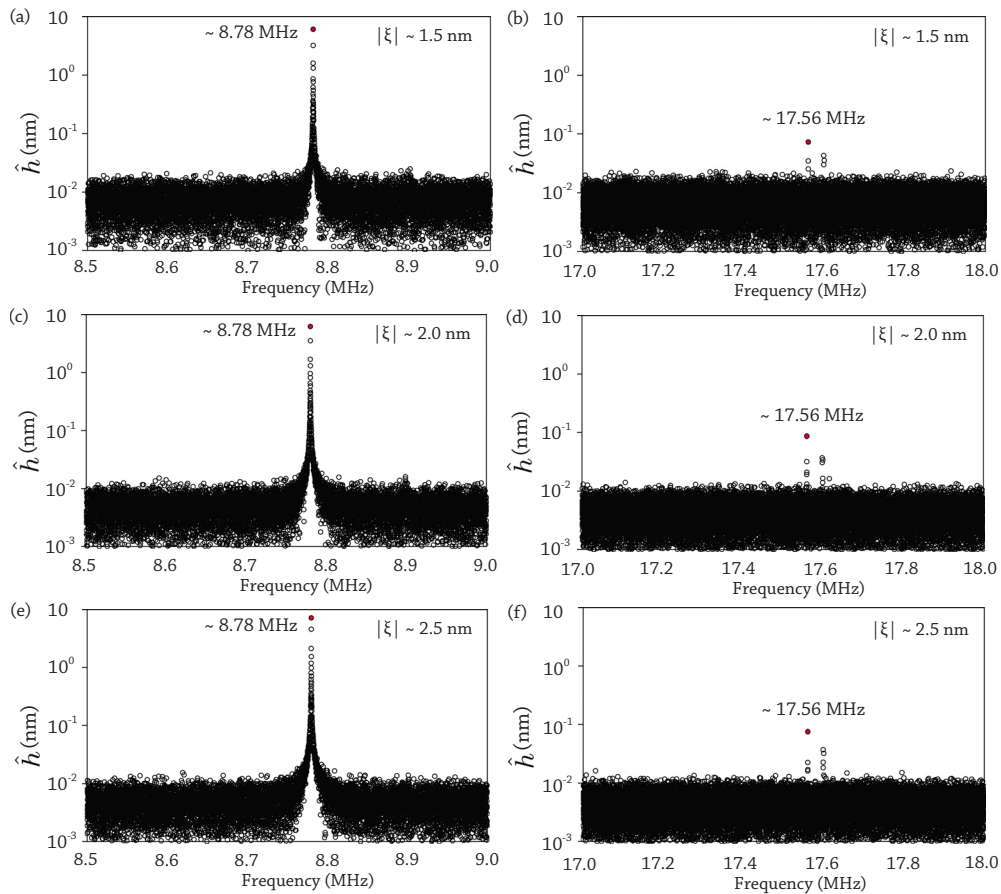
FIG. 9. (Color online) Capillary wave frequency spectra for two different vertical substrate displacement magnitudes measured using the LDV at high megahertz order frequencies—[(a) and (b)] $|\xi| \approx 1.5$ nm, [(c) and (d)] $|\xi| \approx 2.0$ nm, and [(e) and (f)] $|\xi| \approx 2.5$ nm—when driven by an 8.78 MHz SAW. The results show the existence of the first superharmonic frequency $f_1^+ \approx 17.56$ MHz $\approx 2f_0$, where $f_0 = 8.78$ MHz.

part from a linear one with excitation magnitude. Overall, as the SAW magnitude increases from 1.5 to 2.8 nm, the vibration amplitude of the fluid free surface at 20 MHz *decreases* from 2.9 to 0.3 nm. Also, under higher amplitude SAW excitation, the low-frequency broadband vibration of the free surface begins to emerges, as shown in Figs. 8(a)(i), 8(b)(i), 8(c)(i), and 8(d)(i). The frequency band shifts from 10–50 kHz downward to 700–900 Hz when the SAW magnitude is increased from $|\xi| \approx 1.5$ to 2.8 nm, suggesting that the energy appearing at the excitation frequency $f_{SAW} = 20$ MHz is being drawn into the far lower frequency modes via an extended subharmonic period "doubling" sequence.

Due to the limitation of the measurement system and the requirement to maintain the spectra resolution, the spectrum of the first superharmonic frequency for the 20 MHz SAW ($f_1^+ \approx 40$ MHz) exceeds the upper bound of the frequency limit (26 MHz). As such, the existence of the first superharmonic frequency for 20 MHz SAW cannot be verified based on the current experimental setup. However, this problem can be easily resolved by using an 8.78 MHz SAW device *in lieu* of the 20 MHz SAW device. For the case of $f_{SAW} = 8.78$ MHz, we expect $f_0 \approx 8.78$ MHz and $f_1^+ \approx 17.56$ MHz; the first superharmonic frequency is therefore below the upper bound of the measurable frequency range

(26 MHz). Figure 9 shows the frequency spectra of the free surface vibration driven by an 8.78 MHz SAW; Figs. 9(a) and 9(b) $|\xi| \approx 1.5$ nm, Figs. 9(c) and 9(d) $|\xi| \approx 2.0$ nm, and Figs. 9(e) and 9(f) $|\xi| \approx 2.5$ nm. As expected, the results show the existence of the first superharmonic frequency $f_1^+ \approx 17.56$ MHz.

Finally, we speculate that the transition to the regime dominated by subharmonic frequencies, i.e., $\hat{h}(f^-) > \hat{h}(f_0)$ as shown in Figs. 8(d)(i) and 8(d)(ii), is a consequence of the departure from the infinitely small amplitude wave regime and the occurrence of the subharmonic cascade. Using Eq. (56), for 20 MHz acoustic waves, the acoustic Reynolds number for $|\xi| \approx 1.5$, 2, 2.4, and 2.8 nm, is approximately $Re_A \approx 0.7$, 1, 1.2, and 1.4, respectively. However, Re_A does not consider the physical dimension of the liquid film, and therefore it is essential to obtain a different nondimensional parameter that provides a better representation of the significance of the change in the wave magnitude $|\xi|$ and the dimension of the film $\mathcal{H}$. Nondimensionalizing the momentum equation in Eq. (8), assuming the flow to be steady, using the following transformation: $(\mathbf{x}, \mathbf{d}) = \mathfrak{L}(\mathcal{H}/\delta_v)(\tilde{\mathbf{x}}, \tilde{\mathbf{d}})$, $\rho = \rho_{f0}\tilde{\rho}$, and, $\mathbf{u}_2 = \mathcal{U}_2(\mathcal{H}/\delta_v)\tilde{\mathbf{u}}_2$, together with Eq. (10), and selecting terms of order $\mathcal{O}(\varepsilon^2)$ give

$$\mathsf{s}\tilde{\rho}(\tilde{\mathbf{u}}_2 \cdot \boldsymbol{\nabla})\tilde{\mathbf{u}}_2 = \varepsilon^2 \frac{\mu}{\mathfrak{L}\rho_{f0}\mathcal{U}_2}\left[\boldsymbol{\nabla}^2\tilde{\mathbf{u}}_2 + \left(\Lambda + \frac{1}{3}\right)\boldsymbol{\nabla}\,\boldsymbol{\nabla}\cdot\tilde{\mathbf{u}}_2\right],$$

$$(57)$$

where the tilde decoration represents dimensionless quantities, $\mathfrak{L}$ is the characteristic length, $\Lambda = \mu_B/\mu$, and $\mathcal{U}_2$ is the characteristic streaming velocity. The ratio $\mathcal{H}/\delta_v$ captures the way changes in the film height contribute to nonlinear effects, such as the appearance of additional harmonics observed in Fig. 4(d)(ii). We note that this is an important parameter in Liobashevski *et al.*'s study of low-frequency (20–80 Hz) Faraday instabilities. Bifurcation to a subharmonic global pattern (the spatiotemporal behavior of the free surface) is observed for large $\mathcal{H}/\delta_v$ as the acceleration of the fluid layer is increased, whereas propagating solitary structures are observed for small $\mathcal{H}/\delta_v$.[72]

A parameter that captures the onset of fast streaming is defined as $\mathsf{s} = \varepsilon^2(\mathcal{H}/\delta_v)^2$. This is similar to the nonlinear "Reynolds number" $\mathrm{Re}_{\mathrm{NL}} = 2\mathrm{M}_A^2 R^2/\delta_v^2$ introduced by Menguy and Gilbert,[73] for acoustic streaming in a resonator of radius R and acoustic Mach number $\mathrm{M}_A = \mathcal{U}_1/c_0 = \varepsilon$. We further assume that $\mathcal{U}_1 \sim hf_0$ and, therefore, $\varepsilon \sim hf_0/c_0$, where h is the vertical surface displacement of the free surface. In the 20 MHz SAW experiments, $\omega \sim 10^8$ s^{-1}, $\delta_v \sim 10^{-7}$ m, $c_0 \sim 1450$ m/s, and $\mathcal{H} \sim 10^{-3}$ m. Using the recorded time series data, we found that the maximum instantaneous displacement amplitudes for $|\xi| \approx 1.5$, 2.0, 2.4, and 2.8 nm were $h_{\mathrm{max}} \approx 3$, 6, 17, 60 nm, respectively. Therefore, for the cases where $h \sim h_{\mathrm{max}} \approx 3$, 6, 17, and 60 nm, $\mathsf{s} \approx 0.09$, 0.36, 2.9, and 36, respectively, clearly suggesting that the nonlinearity builds quickly as the SAW magnitude increases from 2.4 to 2.8 nm. This is consistent with our speculation that as the amplitude increases beyond a critical level, the energy shifts from the 20 MHz peak to the subharmonic frequencies and subsequently gives rise to the broadening of low-frequency spectra via a subharmonic cascade from the fundamental resonance mode of the free surface. For the 8.78 MHz SAW experiments, $\mathsf{s} < 1$ for all cases shown in Fig. 9, and therefore no flow transition is observed. We note here that the fourth-order nonlinear term $(\tilde{\mathbf{u}}_2 \cdot \boldsymbol{\nabla})\tilde{\mathbf{u}}_2$ is usually neglected in the classical approach.[47,74,75] However, Lighthill[76] pointed out that it is this term that should be retained when the order of magnitude of the viscous term becomes comparable to the inertia term.

IV. DROP

The interesting phenomenon in which $\lambda_c \sim \lambda_{\mathrm{SAW}}$ observed when $\mathcal{L} > \mathcal{H}$, i.e., a film, warrants further investigation, at least to verify that $\lambda_c \neq \lambda_{\mathrm{SAW}}$ when $\mathcal{L} \sim \mathcal{H}$, i.e., a drop. Here, we perform a numerical simulation of a drop subjected to traveling-SAW excitation with the following parameter values: $f_{\mathrm{SAW}} = 20$ MHz, $\mathcal{H} = 1$ mm, and, $\mathcal{L} = 2$ mm. The height $\mathcal{H}$ in Eq. (23) has been redefined as $\mathcal{H}(x) = -2\mathcal{L}^{-1}x^2 + 2x$. In place of the transformation for the case of a film in Eq. (23), we apply the following for the case of a drop:

$$\zeta = x, \quad \eta = \frac{y - [\varepsilon h_1(x,t) + \varepsilon^2 h_2(x,t)]}{\mathcal{H}(x) - [\varepsilon h_1(x,t) + \varepsilon^2 h_2(x,t)]}, \quad (58)$$

where $h_1(x,t)$ and $h_2(x,t)$ are the first and second order surface displacements previously defined in the perturbation expansion of Eq. (24). Substituting Eq. (58) into Eqs. (B1)–(B6), we obtain

$$\frac{\partial}{\partial x} = \frac{\partial}{\partial \zeta} - \frac{\eta_0}{\mathcal{H}}\frac{\partial \mathcal{H}}{\partial \zeta}\frac{\partial}{\partial \eta} + \mathcal{O}(\varepsilon), \quad (59)$$

$$\frac{\partial^2}{\partial x^2} = \frac{\partial^2}{\partial \zeta^2} - \frac{2\eta_0}{\mathcal{H}}\frac{\partial \mathcal{H}}{\partial \zeta}\frac{\partial^2}{\partial \zeta\,\partial \eta} + \frac{2\eta_0^2}{\mathcal{H}^2}\left(\frac{\partial \mathcal{H}}{\partial \zeta}\right)^2\frac{\partial^2}{\partial \eta^2}$$
$$- \frac{\eta_0}{\mathcal{H}}\frac{\partial^2 \mathcal{H}}{\partial \zeta^2}\frac{\partial}{\partial \eta} + \frac{2\eta_0}{\mathcal{H}^2}\left(\frac{\partial \mathcal{H}}{\partial \zeta}\right)^2\frac{\partial}{\partial \eta} + \mathcal{O}(\varepsilon), \quad (60)$$

$$\frac{\partial}{\partial y} = \frac{1}{\mathcal{H}}\frac{\partial}{\partial \eta} + \mathcal{O}(\varepsilon), \quad (61)$$

$$\frac{\partial^2}{\partial y^2} = \frac{1}{\mathcal{H}^2}\frac{\partial^2}{\partial \eta^2} + \mathcal{O}(\varepsilon), \quad (62)$$

$$\frac{\partial^2}{\partial x\,\partial y} = \frac{1}{\mathcal{H}}\frac{\partial^2}{\partial \zeta\,\partial \eta} - \frac{\eta_0}{\mathcal{H}^2}\frac{\partial \mathcal{H}}{\partial \zeta}\frac{\partial^2}{\partial \eta^2} - \frac{1}{\mathcal{H}^2}\frac{\partial \mathcal{H}}{\partial \zeta}\frac{\partial}{\partial \eta}$$
$$- \frac{1}{\mathcal{H}^2}\frac{\partial \mathcal{H}}{\partial \zeta}\frac{\partial}{\partial \zeta} + \mathcal{O}(\varepsilon), \quad (63)$$

$$\frac{\partial}{\partial \tau} = \frac{\partial}{\partial t} + \mathcal{O}(\varepsilon), \quad (64)$$

where $\eta_0 = y/\mathcal{H}$. Next, we combine Eqs. (59)–(64) with Eqs. (13) and (14) to arrive at

$$\frac{\partial \rho_{f1}}{\partial \tau} + \frac{\rho_{f0}}{\mathcal{H}}\frac{\partial u_1^y}{\partial \eta} + \rho_{f0}\frac{\partial u_1^x}{\partial \zeta} - \rho_{f0}\frac{\eta_0}{\mathcal{H}}\frac{\partial \mathcal{H}}{\partial \zeta}\frac{\partial u_1^x}{\partial \eta} = 0, \quad (65)$$

$$\rho_{f0}\frac{\partial u_1^x}{\partial \tau} = \frac{\eta_0}{\mathcal{H}}\frac{\partial \mathcal{H}}{\partial \zeta}\frac{\partial p_1}{\partial \eta} + \frac{2\eta_0}{\mathcal{H}^2}\mu'\left(\frac{\partial \mathcal{H}}{\partial \zeta}\right)^2\frac{\partial u_1^x}{\partial \eta} - \frac{\partial p_1}{\partial \zeta}$$
$$- \frac{\eta_0}{\mathcal{H}}\mu'\frac{\partial^2 \mathcal{H}}{\partial \zeta^2}\frac{\partial u_1^x}{\partial \eta} - \frac{\mu''}{\mathcal{H}^2}\frac{\partial \mathcal{H}}{\partial \zeta}\frac{\partial u_1^y}{\partial \eta} + \frac{\mu}{\mathcal{H}^2}\frac{\partial^2 u_1^x}{\partial \eta^2}$$
$$+ \frac{\eta_0^2}{\mathcal{H}^2}\mu'\left(\frac{\partial \mathcal{H}}{\partial \zeta}\right)^2\frac{\partial^2 u_1^x}{\partial \eta^2} - \frac{\eta_0^2}{\mathcal{H}^2}\mu''\frac{\partial \mathcal{H}}{\partial \zeta}\frac{\partial^2 u_1^y}{\partial \eta^2}$$
$$- \mu''\frac{\partial \mathcal{H}}{\partial \zeta}\frac{\partial u_1^y}{\partial \zeta} - \frac{2\eta_0}{\mathcal{H}}\mu'\frac{\partial \mathcal{H}}{\partial \zeta}\frac{\partial^2 u_1^x}{\partial \zeta\,\partial \eta} + \frac{\mu''}{\mathcal{H}}\frac{\partial^2 u_1^y}{\partial \zeta\,\partial \eta}$$
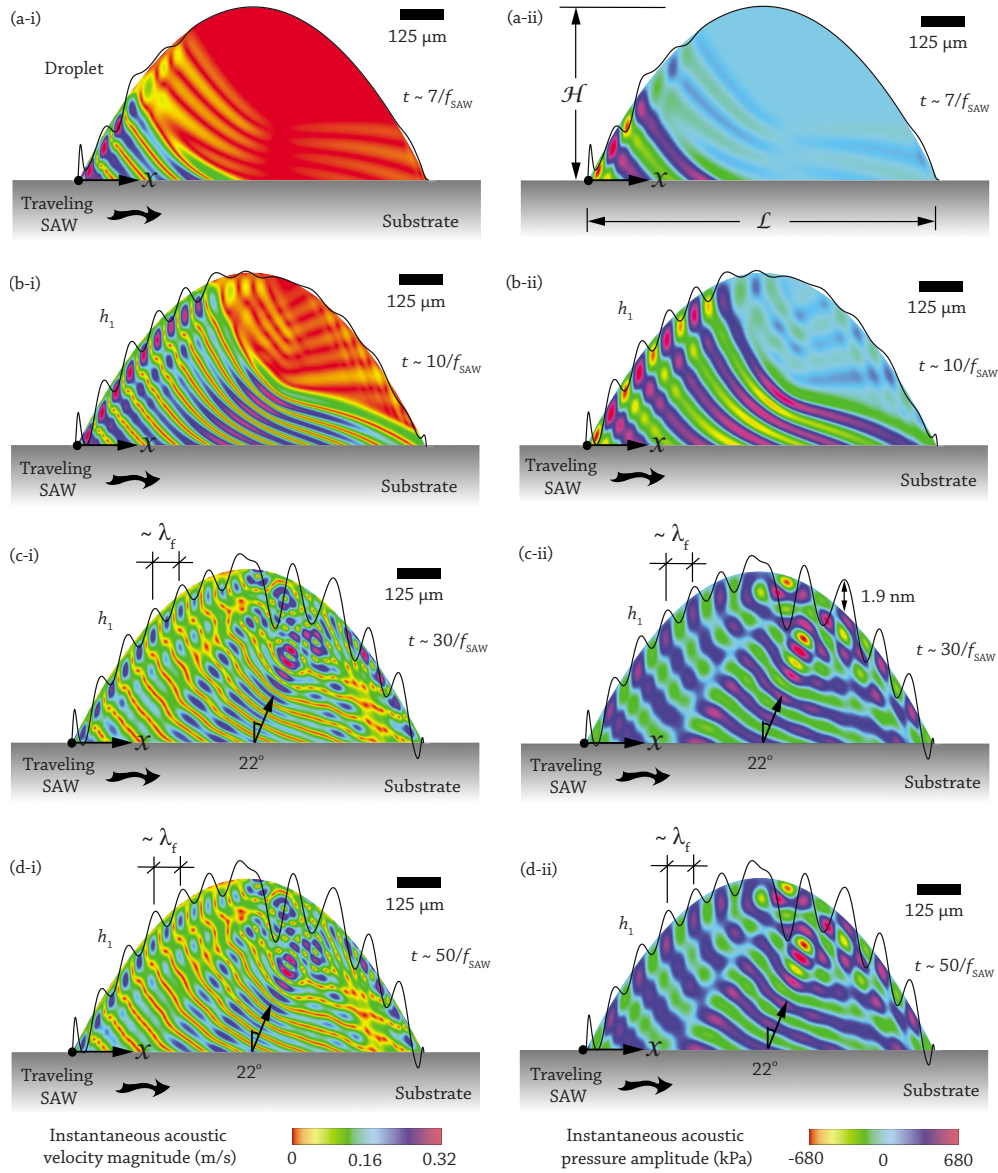$$+ \mu'\frac{\partial^2 u_1^x}{\partial \zeta^2}, \quad (66)$$

FIG. 10. (Color online) Numerical results showing the transmission of acoustic waves into a sessile drop ($\mathcal{H} \sim \mathcal{L}$) at $t=$ [(a)(i) and (a)(ii)] $7f_{SAW}^{-1}$, [(b)(i) and (b)(ii)] $10f_{SAW}^{-1}$, [(c)(i) and (c)(ii)] $30f_{SAW}^{-1}$, and [(d)(i) and (d)(ii)] $50f_{SAW}^{-1}$ s, demonstrating the formation of an acoustic standing wave in the drop along the Rayleigh angle $\theta_R \approx 22°$. The magnitude of the acoustic particle velocity field $|\mathbf{u}_1|$ is shown in (a)(i), (b)(i), (c)(i), and (d)(i), and the amplitude of the acoustic pressure amplitude p_1 is shown in (a)(ii), (b)(ii), (c)(ii), and (d)(ii). The instantaneous displacement h_1 of the free surface has been exaggerated for clarity. The height and diameter of the drop is represented by $\mathcal{H}$ and $\mathcal{L}$, respectively. Thus, for $\mathcal{L} \sim \mathcal{H}$, $\lambda_c \approx \lambda_f$, whereas for $\mathcal{L} > \mathcal{H}$, $\lambda_c \approx \lambda_{SAW}$ (see Fig. 5).

$$\rho_{f0} \frac{\partial u_1^y}{\partial \tau} = -\frac{1}{\mathcal{H}} \frac{\partial p_1}{\partial \eta} - \frac{\mu''}{\mathcal{H}^2} \frac{\partial \mathcal{H}}{\partial \zeta} \frac{\partial u_1^x}{\partial \eta} + \frac{2\eta_0}{\mathcal{H}^2} \mu \left(\frac{\partial \mathcal{H}}{\partial \zeta} \right)^2 \frac{\partial u_1^y}{\partial \eta}$$

$$- \frac{\eta_0}{\mathcal{H}} \mu \frac{\partial^2 \mathcal{H}}{\partial \zeta^2} \frac{\partial u_1^y}{\partial \eta} - \frac{\eta_0}{\mathcal{H}^2} \mu'' \frac{\partial \mathcal{H}}{\partial \zeta} \frac{\partial^2 u_1^x}{\partial \eta^2} + \frac{\mu'}{\mathcal{H}^2} \frac{\partial^2 u_1^y}{\partial \eta^2}$$

$$+ \frac{\eta_0^2}{\mathcal{H}^2} \mu \left(\frac{\partial \mathcal{H}}{\partial \zeta} \right)^2 \frac{\partial^2 u_1^y}{\partial \eta^2} - \frac{\mu''}{\mathcal{H}^2} \frac{\partial \mathcal{H}}{\partial \zeta} \frac{\partial u_1^x}{\partial \zeta} + \frac{\mu''}{\mathcal{H}} \frac{\partial^2 u_1^x}{\partial \zeta \partial \eta}$$

$$- \frac{2\eta_0}{\mathcal{H}} \mu \frac{\partial \mathcal{H}}{\partial \zeta} \frac{\partial^2 u_1^y}{\partial \zeta \partial \eta} + \mu \frac{\partial^2 u_1^y}{\partial \zeta^2}. \tag{67}$$

The boundary conditions at the free surface and solid-fluid interface remain unchanged. Under low excitation power, the drop is observed in all previous experiments to be essentially pinned at the contact line. Therefore, at the contact line, the

following boundary conditions are prescribed: $h_1=0$, $u_1^x=0$, and, $u_1^y=0$ at $x=0$ and $x=\mathcal{L}$. The results for the film in Figs. 5(a)(ii) and 5(a)(iii) show that the contribution of the second-order field to the surface deformation profile h is insignificant. As such, the present drop model only involves solving the first-order equations.

As shown in Fig. 10, the numerical results for drops with $\mathcal{L} \sim \mathcal{H}$ show that an acoustic standing wave is formed predominantly along the radiation angle $\theta_R \approx 22°$ and that the distance between two pressure nodal points on the free surface is approximately $\lambda_f/2$. In order to illustrate the interference of acoustic waves within a drop more clearly, we use a 20 MHz pulse mode excitation (one cycle on and four cycles off of a sinusoidal signal) and extract the first-order results at $t = 8f_{SAW}^{-1}$, $9f_{SAW}^{-1}$, $10f_{SAW}^{-1}$, $11f_{SAW}^{-1}$, $12f_{SAW}^{-1}$, $13f_{SAW}^{-1}$, $14f_{SAW}^{-1}$,
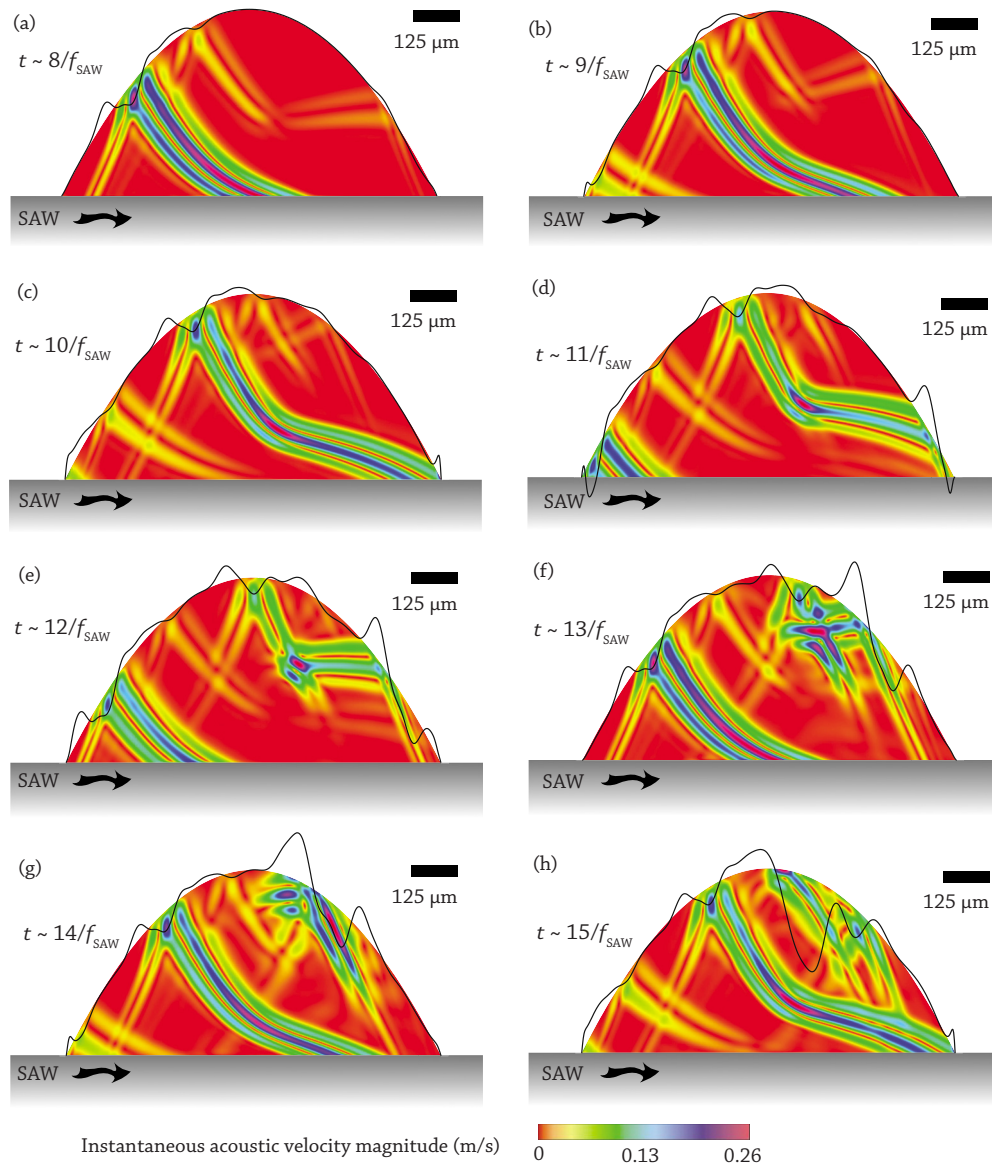
FIG. 11. (Color online) Numerical results showing the propagation/reflection of acoustic waves in a sessile drop ($\mathcal{H} \sim \mathcal{L}$) at $t=$ (a) $8f_{SAW}^{-1}$, (b) $9f_{SAW}^{-1}$, (c) $10f_{SAW}^{-1}$, (d) $11f_{SAW}^{-1}$, (e) $12f_{SAW}^{-1}$, (f) $13f_{SAW}^{-1}$, (g) $14f_{SAW}^{-1}$, and (h) $15f_{SAW}^{-1}$ s, under a 20 MHz pulse mode excitation (one cycle on and four cycles off of a sinusoidal signal). The results show the complex interaction between the incident and reflected waves within the drop, and therefore no phase-locking mechanism arises. In addition, the motion of the free surface under pulse mode excitation is irregular and no specific λ_c can be identified. The instantaneous displacement h_1 of the free surface has been exaggerated for clarity.

and $15f_{SAW}^{-1}$ seconds, as shown in Figs. 11(a)–11(h), respectively. The results show that the interaction of acoustic waves within a drop is far more complex compared to that in the case of a film (Fig. 6); further, the grid-structure formed by the superposed waves is absent, suggesting no phase-locking mechanism is possible and therefore $\lambda_c \neq \lambda_{SAW}$. The drop model presented here, however, is essentially valid for low-amplitude SAW ($Re_A < 1$) and therefore unable to capture the apparent deformation ($\lambda_c \sim R_d$) of the free surface. Nonetheless, capturing the formation of the acoustic standing wave along the Rayleigh angle $\theta_R \approx 22°$ generated by a traveling SAW is consistent with the previously reported experimental observation in which a rapid microjet along the Rayleigh angle is generated by a high intensity traveling SAW.[13] Furthermore, the results also show that polygonlike structures are formed at the top-right corner of the drop due to the

superposition of the incident and reflected acoustic waves (Fig. 10), consistent with Brunet *et al.*'s[52] numerical results.

Finally, we provide a direct qualitative comparison between experimental and numerical results by presenting a case study that analyzes the alignment of microparticles on a hemispherical sessile drop. A consequence of standing capillary waves is the assembly of hydrophobic particles along antinodal displacement lines.[77] To reduce the effect of acoustic streaming on the particles, the amplitude of SAW needs to be sufficiently low ($\xi \ll 1$ nm), such that the net flow of the fluid can be neglected. In the experiments, the substrate was coated with a layer of hydrophobic material (Teflon AF, DuPont Corp., Wilmington, Delaware), and therefore the drop shape is almost hemispherical with a contact angle of approximately 118°. The motion of 6 μm fluorescent polystyrene (hydrophobic) particles (Duke Scientific, Palo Alto,

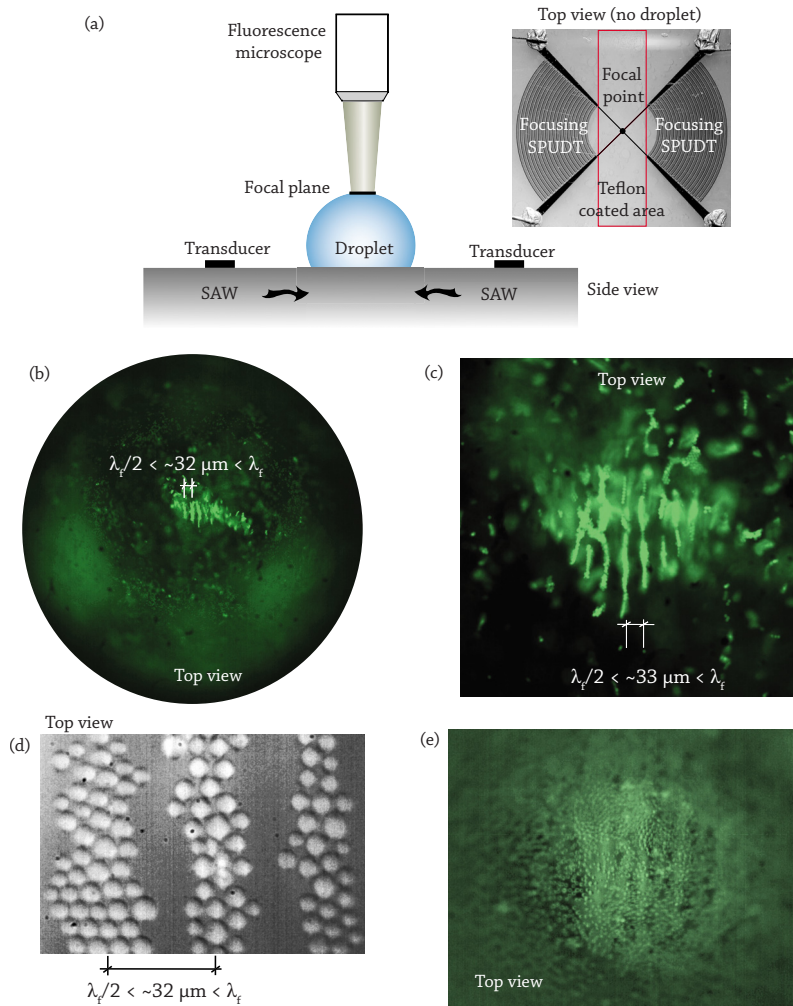FIG. 12. (Color online) (a) Schematic of the experimental setup used to visualize the collection of 6 μm particles on a 3 $\mu\ell$ drop ($\mathcal{H} \sim \mathcal{L}$) due to the vibration of its free surface using 30 MHz standing SAWs generated by two focusing SPUDTs. The images—captured with (b) 5×, (c) 10×, and (d) 50× microscope lenses—show that the microparticles are collected at the top of the drop (focal plane). The distance δ_{St} between two adjacent collection lines is 32±4 μm, therefore falling within the limits of $\lambda_f/2 < \delta_{St} < \lambda_f$, where $\lambda_f \approx 49$ μm for 30 MHz acoustic waves in water. (e) The aligned particles are dispersed and move along the streamlines (or accumulate at the apex of the drop) when the amplitude of SAW is increased.

CA) suspended in the drop was observed under fluorescence microscopy (BXFM stereomicroscope and iSpeed camera, Olympus, Japan) at 500 frames/s. Figure 12(a) illustrates the experimental setup. The excitation frequency was 30 MHz and hence $\lambda_{SAW} \approx 130$ μm and $\lambda_f \approx 49$ μm. Two focusing single-phase unidirectional transducers were used to generate high intensity focusing standing SAWs. We note that this type of SAW device has been used to generate slender SAW microjet in previous studies.[13] Under extremely low excitation power ($\xi \ll 1$ nm), the particles are observed to align on top of a $3\mu\ell$ droplet ($\mathcal{H} \sim \mathcal{L}$) with the distance δ_{St} between two adjacent alignment lines varying in the range between $\delta_{St} = 32 \pm 4$ μm; therefore, $\lambda_f/2 < \delta_{St} < \lambda_f$, as shown in Figs. 12(b)–12(d). With only a slight increase in the amplitude of SAW, the aligned particles are observed to be dispersed and are seen to move along the streamlines (or to accumulate at the apex of the drop) as a consequence of the buildup of slow streaming, as shown in Fig. 12(d).

It is then possible to use the numerical model developed above to verify the formation of acoustic standing waves and, hence, to verify the δ_{St} separation along the free surface for a drop of radius $R_d = 500$ μm under 30 MHz standing SAW excitation. Since the amplitude of SAW is extremely low ($\xi \ll 1$ nm and hence $\text{Re}_A \ll 1$), it is therefore possible to neglect the $\mathcal{O}(\varepsilon^2)$ contributions—only $\mathcal{O}(\varepsilon)$ contributions

are considered. Figure 13 shows the numerical results of the acoustic velocity magnitude $|\mathbf{u}_1|$ and the acoustic pressure p_1 field in the drop after $t = 15 f_{SAW}^{-1}$ and $30 f_{SAW}^{-1}$ s. Near the drop apex, the distance δ_{St} between two adjacent displacement antinodal points is within the limits of $\lambda_f/2 < \delta_{St} < \lambda_f$, consistent with the experimental results. Therefore, it appears that for $\mathcal{H} \sim \mathcal{L}$, the distance between two adjacent displacement antinodes lines is associated with the acoustic wavelength of the liquid.

V. CONCLUSIONS

A combination of both numerical and experimental studies has been presented to capture the salient features of the free surface dynamics of a liquid vibrating under high frequency surface acoustic wave excitation. A two-dimensional numerical model was constructed that couples the motion of the piezoelectric substrate and a thin liquid layer atop the substrate from both the solid to the fluid and vice versa. For the solid domain, the time-domain constitutive equations that describe the motion of the piezoelectric substrate were employed. For the fluid domain, the assumption of infinitesimally small amplitude acoustic waves was employed, which then permitted the use of successive approximations to decompose the equations governing the fluid motion such that
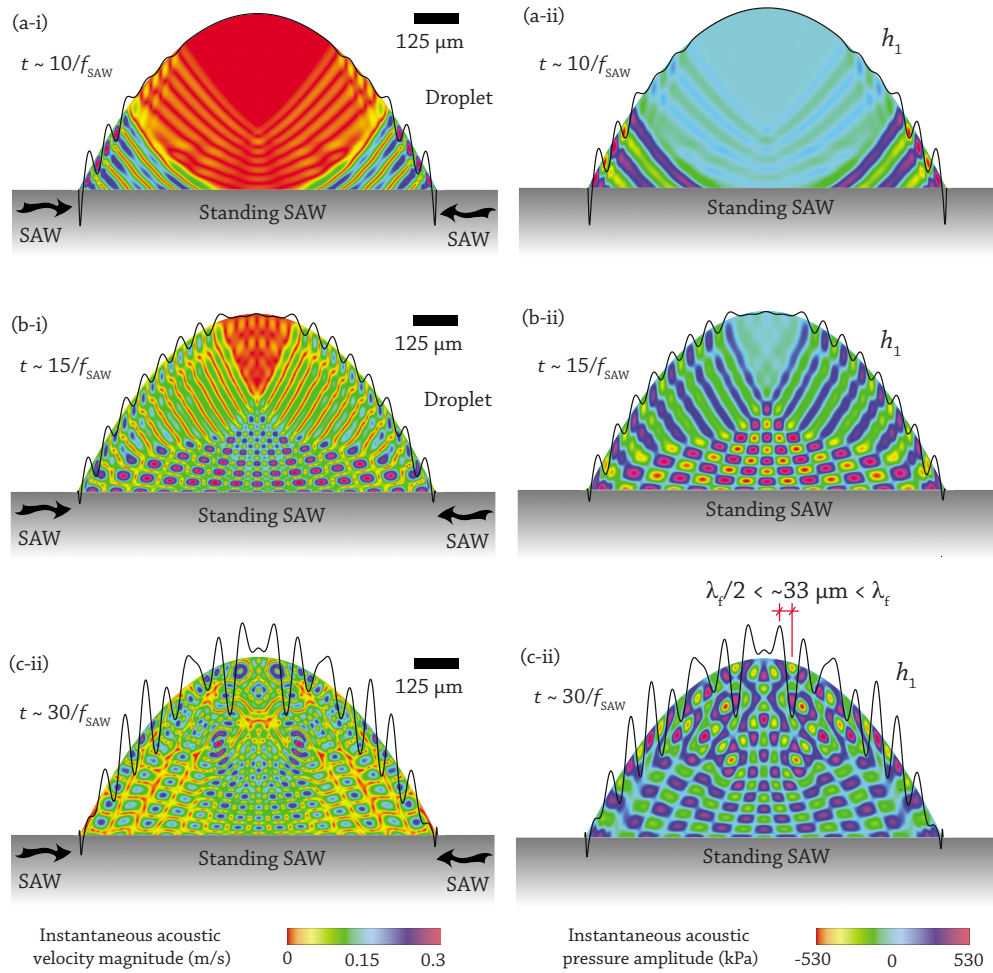
FIG. 13. (Color online) Numerical results showing the transmission of 30 MHz standing SAWs into a sessile drop ($\mathcal{H} \sim \mathcal{L}$) at $t=$ [(a)(i) and (a)(ii)] $10f_{SAW}^{-1}$, [(b)(i) and (b)(ii)] $15f_{SAW}^{-1}$, and [(c)(i) and (c)(ii)] $30f_{SAW}^{-1}$ s; (a)(i), (b)(i), and (c)(i) are the instantaneous acoustic velocity magnitude $|\mathbf{u}_1|$ plots, whereas (a)(ii), (b)(ii), and (c)(ii) are the instantaneous acoustic pressure amplitude p_1 plots. The results suggest that on the top of the drop, the distance between two adjacent displacement antinodal lines (δ_{St}) is $\lambda_f/2 < \delta_{St} \approx 33$ μm $< \lambda_f$, consistent with the experimental results in Figs. 12(b)–12(d).

it can be resolved at the two widely varying time scales relevant to the problem. Due to this method of successive approximation, the numerical model is, however, limited to the study of free surface dynamics in the low-amplitude flow regime ($Re_A < 1$). We thus augment the study with experiments to capture the free surface dynamics in the high-amplitude flow regime ($Re_A > 1$). Together, the combined numerical and experimental studies therefore offer a basis upon which the free surface dynamics driven by surface acoustic waves across the entire range of excitation amplitudes from low Re_A to high Re_A can be analyzed.

In both the simulations and experiments, a time series data of the free surface deformation h were captured. The results revealed that the flow regime had a critical influence on the dynamics of the free surface. For the low-amplitude flow regime ($Re_A < 1$), only a single peak was found in the frequency spectra. The resonant frequency of the free surface, in this case, is identical to the frequency of the SAW ($f_c \approx f_{SAW}$), consistent with previous experimental results. The omission of strong nonlinear terms as well as the small free surface assumption ($\varepsilon h_2 \ll h_1$) required by the numerical model therefore cannot capture the behavior of the large amplitude flow regime ($Re_A > 1$), where strong nonlinear effects

become dominant, resulting in a shift of acoustic energy from a single peak at f_{SAW} to a low-frequency broadband spectra. This phenomenon is associated with the emergence of fast streaming. A simple scaling analysis of the leading order terms in the momentum equation further shows the importance of such strong nonlinearity arising from the higher order terms, which is postulated to be the reason for the low-frequency broadband vibration. A nonlinear parameter is derived to define the onset of such strong nonlinear effects; i.e., when $\varsigma > 1$.

The results of the numerical simulation, however, are able to provide insight into the $\lambda_{SAW}/2$ separation distance between two adjacent displacement nodal points on the free surface reported in Li *et al.*[63] and Alvarez *et al.*;[20] the former observed that particles suspended on the free surface collect at displacement nodal lines, whereas the latter reported the formation of polymer spot patterns, also along displacement nodal lines. Thus, despite the simplicity of our numerical model, the results are able to capture these salient features observed in experiments, suggesting that they occur as a result of phase-locking of the vertical component of the velocities; that is, the phases of u^y at $y=0$ and at $y=\mathcal{H}$ along the x-axis are closely matched. The numerical results further re-

veal that the separation distance depends on the geometry of the system: for a film where $\mathcal{L} > \mathcal{H}$, the separation distance approaches $\lambda_{SAW}/2$, whereas for a drop where $\mathcal{L} \sim \mathcal{H}$, the separation distance approaches $\lambda_f/2$.

The close agreement between the predictions afforded by our simple model and the experimental results lends confidence to the numerical model for the prediction of the flow field under low excitation amplitudes. Good agreement was obtained between experiments and numerics, in that, (1) the fundamental resonant frequency of the free surface is identical to the excitation frequency, i.e., $f_0 = f_{SAW}$, (2) the separation distance between two adjacent pressure nodal points on the free surface of a film ($\mathcal{L} > \mathcal{H}$) is approximately $\lambda_{SAW}/2$ excited by a traveling-SAW, and (3) the separation distance between two adjacent displacement antinodal points on the free surface of a hemispherical drop ($\mathcal{L} \sim \mathcal{H}$) is within the range of $\lambda_f/2$ excited by a standing SAW. Finally, the existence of superharmonic frequency $f_1^+ \approx 2f_0$ has also been shown. The present results offer guidance for the numerical study of SAW atomization, which involves the use of large excitation powers to drive the transition from the slow streaming regime ($Re_A < 1$) into the fast streaming regime ($Re_A > 1$), in anticipation of a more complex numerical scheme that spans both regimes and fully satisfies the large amplitude capillary wave vibrations that proceed toward pinch-off and droplet breakup.

APPENDIX A: TRANSFORMED MATERIAL PROPERTIES

The transformed piezoelectric constant e_{kij}, dielectric constant ϵ_{ik}^S, and elastic stiffness constant c_{ijkl}^E for 128° YX lithium niobate (LiNbO$_3$, LN) are[53]

$$[e] = \begin{bmatrix} 0 & 0 & 0 & 0 & 4.46 & 0.4 \\ -1.77 & 4.46 & -1.59 & 0.12 & 0 & 0 \\ 1.68 & -2.67 & 2.4 & 0.59 & 0 & 0 \end{bmatrix} \frac{C}{m^2}, \quad \text{(A1)}$$

$$[\epsilon] = \begin{bmatrix} 44 & 0 & 0 \\ 0 & 37.9 & -7.81 \\ 0 & -7.81 & 34 \end{bmatrix} \frac{F}{m}, \quad \text{(A2)}$$

$$[c] = \begin{bmatrix} 20.3 & 7.23 & 6.02 & 1.07 & 0 & 0 \\ 7.23 & 19.4 & 9.06 & 0.89 & 0 & 0 \\ 6.02 & 9.06 & 22.03 & 0.81 & 0 & 0 \\ 1.07 & 0.89 & 0.81 & 7.49 & 0 & 0 \\ 0 & 0 & 0 & 0 & 5.63 & -0.44 \\ 0 & 0 & 0 & 0 & -0.44 & 7.6 \end{bmatrix} 10^{10} \frac{N}{m^2}. \quad \text{(A3)}$$

APPENDIX B: COORDINATE TRANSFORMATION

The following general transformation of the partial derivatives from a physical space (x, y, t) to a computational space (ζ, η, τ) for a two-dimensional unsteady flow is used:[61]

$$\frac{\partial}{\partial x} = \frac{\partial}{\partial \zeta}\left(\frac{\partial \zeta}{\partial x}\right) + \frac{\partial}{\partial \eta}\left(\frac{\partial \eta}{\partial x}\right), \quad \text{(B1)}$$

$$\frac{\partial^2}{\partial x^2} = \frac{\partial}{\partial \zeta}\left(\frac{\partial^2 \zeta}{\partial x^2}\right) + \frac{\partial}{\partial \eta}\left(\frac{\partial^2 \eta}{\partial x^2}\right) + \frac{\partial^2}{\partial \zeta^2}\left(\frac{\partial \zeta}{\partial x}\right)^2 + \frac{\partial^2}{\partial \eta^2}\left(\frac{\partial \eta}{\partial x}\right)^2$$
$$+ 2\frac{\partial^2}{\partial \eta \partial \zeta}\left(\frac{\partial \eta}{\partial x}\right)\left(\frac{\partial \zeta}{\partial x}\right), \quad \text{(B2)}$$

$$\frac{\partial}{\partial y} = \frac{\partial}{\partial \zeta}\left(\frac{\partial \zeta}{\partial y}\right) + \frac{\partial}{\partial \eta}\left(\frac{\partial \eta}{\partial y}\right), \quad \text{(B3)}$$

$$\frac{\partial^2}{\partial y^2} = \frac{\partial}{\partial \zeta}\left(\frac{\partial^2 \zeta}{\partial y^2}\right) + \frac{\partial}{\partial \eta}\left(\frac{\partial^2 \eta}{\partial y^2}\right) + \frac{\partial^2}{\partial \zeta^2}\left(\frac{\partial \zeta}{\partial y}\right)^2 + \frac{\partial^2}{\partial \eta^2}\left(\frac{\partial \eta}{\partial y}\right)^2$$
$$+ 2\frac{\partial^2}{\partial \eta \partial \zeta}\left(\frac{\partial \eta}{\partial y}\right)\left(\frac{\partial \zeta}{\partial y}\right), \quad \text{(B4)}$$

$$\frac{\partial^2}{\partial x \partial y} = \frac{\partial}{\partial \zeta}\left(\frac{\partial^2 \zeta}{\partial x \partial y}\right) + \frac{\partial}{\partial \eta}\left(\frac{\partial^2 \eta}{\partial x \partial y}\right) + \frac{\partial^2}{\partial \zeta^2}\left(\frac{\partial \zeta}{\partial x}\right)\left(\frac{\partial \zeta}{\partial y}\right)$$
$$+ \frac{\partial^2}{\partial \eta^2}\left(\frac{\partial \eta}{\partial x}\right)\left(\frac{\partial \eta}{\partial y}\right) + \frac{\partial^2}{\partial \zeta \partial \eta}\left[\left(\frac{\partial \eta}{\partial x}\right)\left(\frac{\partial \zeta}{\partial y}\right)\right.$$
$$\left. + \left(\frac{\partial \zeta}{\partial x}\right)\left(\frac{\partial \eta}{\partial y}\right)\right], \quad \text{(B5)}$$

$$\frac{\partial}{\partial t} = \frac{\partial}{\partial \zeta}\left(\frac{\partial \zeta}{\partial t}\right) + \frac{\partial}{\partial \eta}\left(\frac{\partial \eta}{\partial t}\right) + \frac{\partial}{\partial \tau}\left(\frac{\partial \tau}{\partial t}\right). \quad \text{(B6)}$$

[1] L. Y. Yeo and J. R. Friend, "Ultrafast microfluidics using surface acoustic waves," Biomicrofluidics **3**, 012002 (2009).

[2] H. Li, J. R. Friend, and L. Y. Yeo, "Surface acoustic wave concentration of particle and bioparticle suspensions," Biomed. Microdevices **9**, 647 (2007).

[3] R. Shilton, M. K. Tan, L. Y. Yeo, and J. R. Friend, "Particle concentration and mixing in microdrops driven by focused surface acoustic waves," J. Appl. Phys. **104**, 014910 (2008).

[4] W. K. Tseng, J. L. Lin, W. C. Sung, S. H. Chen, and G. B. Lee, "Active micro-mixers using surface acoustic waves on Y-cut 128° LiNbO$_3$," J. Micromech. Microeng. **16**, 539 (2006).

[5] M. Cecchini, S. Girardo, D. Pisignano, R. Cingolani, and F. Beltram, "Acoustic-counterflow microfluidics by surface acoustic waves," Appl. Phys. Lett. **92**, 104103 (2008).

[6] M. K. Tan, L. Y. Yeo, and J. R. Friend, "Rapid microchannel fluid actuation and particle manipulation induced by surface acoustic waves," Europhys. Lett. **87**, 47003 (2009).

[7] G. McHale, M. K. Banerjee, and M. I. Newton, "Surface acoustic wave resonances in the spreading of viscous fluids," Phys. Rev. B **59**, 8262 (1999).

[8] A. Wixforth, C. Strobl, C. Gauer, A. Toegl, J. Scriba, and Z. v. Guttenberg, "Acoustic manipulation of small droplets," Anal. Bioanal. Chem. **379**, 982 (2004).

[9] M. K. Tan, J. R. Friend, and L. Y. Yeo, "Microparticle collection and concentration via a miniature surface acoustic wave device," Lab Chip **7**, 618 (2007).

[10] N. Shimizu, J. Kondoh, Y. Matsui, and S. Shiokawa, "Localized heating effects of liquid based on saw streaming," *Proceedings of the 2004 IEEE Ultrasonics Symposium* (IEEE, Los Alamitos, CA, 2004), Vol. 3, pp. 2235–2238.

[11] J. Kondoh, N. Shimizu, Y. Matsui, M. Sugimoto, and S. Shiokawa, "Development of temperature-control system for liquid droplet using surface acoustic wave devices," Sens. Actuators, A **149**, 292 (2009).

[12] K. Kulkarni, J. Friend, L. Yeo, and P. Perlmutter, "Surface acoustic waves as an energy source for drop scale synthetic chemistry," Lab Chip **9**, 754 (2009).

[13] M. K. Tan, J. R. Friend, and L. Y. Yeo, "Interfacial jetting phenomena induced by focused surface vibrations," Phys. Rev. Lett. **103**, 024501 (2009).

[14] M. Kurosawa, T. Watanabe, A. Futami, and T. Higuchi, "Surface acoustic wave atomizer," Sens. Actuators, A **50**, 69 (1995).

[15] K. Chono, N. Shimizu, Y. Matsui, J. Kondoh, and S. Shiokawa, "Development of novel atomization system based on SAW streaming," Jpn. J. Appl. Phys. **43**, 2987 (2004).

[16] A. Qi, L. Y. Yeo, and J. R. Friend, "Interfacial destabilization and atomization driven by surface acoustic waves," Phys. Fluids **20**, 074103 (2008).

[17] J. W. Kim, Y. Yamagata, M. Takasaki, B. H. Lee, H. Ohmori, and T. Higuchi, "A device for fabricating protein chips by using surface acoustic wave atomizer and electrostatic deposition," Sens. Actuators B **107**, 535 (2005).

[18] M. Alvarez, J. Friend, and L. Y. Yeo, "Rapid generation of protein aerosols and nanoparticles via surface acoustic wave atomization," Nanotechnology **19**, 455103 (2008).

[19] A. Qi, J. R. Friend, L. Y. Yeo, D. A. V. Morton, M. P. McIntosh, and L. Spiccia, "Miniature inhalation therapy platform using surface acoustic wave microfluidic atomization," Lab Chip **9**, 2184 (2009).

[20] M. Alvarez, J. Friend, and L. Y. Yeo, "Surface vibration induced spatial ordering of periodic polymer patterns on a substrate," Langmuir **24**, 10629 (2008).

[21] A. Qi, L. Y. Yeo, J. R. Friend, and J. Ho, "The extraction of liquid, protein molecules and yeast cells from paper through surface acoustic wave atomization," Lab Chip **10**, 470 (2010).

[22] M. Faraday, "On a peculiar class of acoustical figures; and on certain forms assumed by groups of particles upon vibrating elastic surfaces," Philos. Trans. R. Soc. London **121**, 299 (1831).

[23] T. B. Benjamin and F. Ursell, "The stability of the plane free surface of a liquid in vertical periodic motion," Proc. R. Soc. London, Ser. A **225**, 505 (1954).

[24] W. Eisenmenger, "Dynamic properties of the surface tension of water and aqueous solutions of surface active agents with standing capillary waves in the frequency range from 10 Kc/S to 1.5 Mc/S," Acustica **9**, 327 (1959).

[25] J. Miles and D. Henderson, "Parametrically forced surface waves," Annu. Rev. Fluid Mech. **22**, 143 (1990).

[26] K. Kumar and L. S. Tuckerman, "Parametric instability of the interface between two fluids," J. Fluid Mech. **279**, 49 (1994).

[27] K. Kumar, "Linear theory of Faraday instability in viscous liquids," Proc. R. Soc. London, Ser. A **452**, 1113 (1996).

[28] H. W. Müller, H. Wittmer, C. Wagner, J. Albers, and K. Knorr, "Analytic stability theory for Faraday waves and the observation of the harmonic surface response," Phys. Rev. Lett. **78**, 2357 (1997).

[29] R. Keolian, L. A. Turkevich, S. J. Putterman, and I. Rudnick, "Subharmonic sequences in the Faraday experiment: departures from period doubling," Phys. Rev. Lett. **47**, 1133 (1981).

[30] P. Chen and J. Viñals, "Amplitude equation and pattern selection in Faraday waves," Phys. Rev. E **60**, 559 (1999).

[31] A. M. Rucklidge, "Pattern formation in large domains," Philos. Trans. R. Soc. London, Ser. A **361**, 2649 (2003).

[32] J. Lighthill, *Waves in Fluids* (Cambridge University, Cambridge, 1978).

[33] M. S. Longuet-Higgins, "The instabilities of gravity waves of finite amplitude in deep water: I. Superharmonics," Proc. R. Soc. London, Ser. A **360**, 471 (1978).

[34] M. S. Longuet-Higgins, "The instabilities of gravity waves of finite amplitude in deep water: I. Subharmonics," Proc. R. Soc. London, Ser. A **360**, 489 (1978).

[35] J. Lucassen, "Longitudinal capillary waves. Part 1—Theory," Trans. Faraday Soc. **64**, 2221 (1968).

[36] J. Lucassen, "Longitudinal capillary waves. Part 2—Experiment," Trans. Faraday Soc. **64**, 2230 (1968).

[37] J. A. De Feijter, "The propagation of surface shear waves: 1. Theory," J. Colloid Interface Sci. **69**, 375 (1979).

[38] D. Sharp, "An overview of Rayleigh-Taylor instability," Physica D **12**, 3 (1984).

[39] O. Lioubashevski, J. Fineberg, and L. S. Tuckerman, "Scaling of the transition to parametrically driven surface waves in highly dissipative systems," Phys. Rev. E **55**, R3832 (1997).

[40] E. Cerda and E. Tirapegui, "Faraday's instability in viscous fluid," J. Fluid Mech. **368**, 195 (1998).

[41] S. Kumar, "Mechanism for the Faraday instability in viscous liquids," Phys. Rev. E **62**, 1416 (2000).

[42] A. J. James, B. Vukasinovic, M. K. Smith, and A. Glezer, "Vibration-induced drop atomization and bursting," J. Fluid Mech. **476**, 1 (2003).

[43] M. Y. Brazhnikov, G. V. Kolmakov, A. A. Levchenko, and L. P. Mezhov-Deglin, "Observation of capillary turbulence on the water surface in a wide range of frequencies," Europhys. Lett. **58**, 510 (2002).

[44] K. Naugolnykh and L. Ostrovsky, *Nonlinear Wave Processes in Acoustics* (Cambridge University, Cambridge, 1998).

[45] M. Schindler, P. Talker, and P. Hänggi, "Computing stationary free-surface shapes in microfluidics," Phys. Fluids **18**, 103303 (2006).

[46] D. Köster, "Numerical simulation of acoustic streaming on surface acoustic wave-driven biochips," SIAM J. Sci. Comput. (USA) **29**, 2352 (2007).

[47] W. L. Nyborg, in *Acoustic Streaming*, edited by W. P. Mason and R. N. Thurston (Academic, San Diego, CA, 1965), Chap. 11, pp. 265–329.

[48] L. D. Rozenberg, *High-Intensity Ultrasonic Fields* (Plenum, New York, 1971).

[49] P. M. Morse and K. U. Ingard, *Theoretical Acoustics* (McGraw-Hill, New York, 1968).

[50] C. E. Bradley, "Acoustic streaming field structure: The influence of the radiator," J. Acoust. Soc. Am. **100**, 1399 (1996).

[51] L. Dong, A. Chaudhury, and M. K. Chaudhury, "Lateral vibration of a water drop and its motion on a vibrating surface," Eur. Phys. J. E **21**, 231 (2006).

[52] P. Brunet, M. Baudoin, O. B. Matar, and F. Zoueshtiagh, "Droplet displacements and oscillations induced by ultrasonic surface acoustic waves: A qualitative study," Phys. Rev. E **81**, 036315 (2010).

[53] B. A. Auld, *Acoustic Fields and Waves in Solids* (Wiley, New York, 1973), Vol. 1.

[54] H. F. Tiersten, "Wave propagation in an infinite piezoelectric plate," J. Acoust. Soc. Am. **35**, 234 (1963).

[55] F. Chagla and P. M. Smith, "Finite difference time domain methods for piezoelectric crystals," IEEE Trans. Ultrason. Ferroelectr. Freq. Control **53**, 1895 (2006).

[56] R. T. Beyer, in *Nonlinear Acoustics: The Parameter B/A*, edited by M. F. Hamilton and D. T. Blackstock (Academic, New York, 1998), Chap. 2, pp. 25–40.

[57] F. V. Hunt, "Notes on the exact equations governing the propagation of sound in fluids," J. Acoust. Soc. Am. **27**, 1019 (1955).

[58] C. T. Schröder and W. R. Scott, "A finite-difference model to study the elastic wave interaction with buried land mines," IEEE Trans. Geosci. Remote Sens. **38**, 1505 (2000).

[59] F. Collino and C. Tsogko, "Application of the perfectly matched absorbing layer model to the linear elastodynamic problem in anisotropic heterogeneous media," Geophysics **66**, 294 (2001).

[60] D. Botteldooren, "Vorticity and entropy boundary conditions for acoustical finite-difference time-domain simulations," J. Acoust. Soc. Am. **102**, 170 (1997).

[61] J. D. Anderson, *Computational Fluid Dynamics: The Basics with Application* (McGraw-Hill, New York, 1995), p. 261.

[62] O. V. Rudenko and S. I. Soluyan, *Theoretical Foundations of Nonlinear Acoustics* (Consultants Bureau, New York, 1977).

[63] H. Li, J. R. Friend, and L. Y. Yeo, "Microfluidic colloidal island formation and erasure induced by surface acoustic wave radiation," Phys. Rev. Lett. **101**, 084502 (2008).

[64] A. D. Heathershaw, "Seabed-wave resonance and sand bar growth," Nature (London) **296**, 343 (1982).

[65] C. Sarasola, F. J. Torrealdea, A. d'Anjou, A. Moujahid, and M. Graña, "Energy balance in feedback synchronization of chaotic systems," Phys. Rev. E **69**, 011606 (2004).

[66] D. Binks, M. T. Westra, and W. van de Water, "Effect of depth on the pattern formation of Faraday waves," Phys. Rev. Lett. **79**, 5010 (1997).

[67] B. Christiansen and M. T. Alstrøm Levinsen, "Ordered capillary-wave states: quasicrystals, hexagons, and radial waves," Phys. Rev. Lett. **68**, 2157 (1992).

[68] H. Arbell and J. Fineberg, "Pattern formation in two-frequency parametric waves," Phys. Rev. E **65**, 036224 (2002).

[69] C. K. Campbell, *Surface Acoustic Wave Devices* (Academic, London, 1988).

[70] K. Y. Hashimoto, *Surface Acoustic Wave Devices in Telecommunications* (Springer-Verlag, Berlin, 2000).

[71] J. Friend and L. Yeo, "Using laser Doppler vibrometry to measure capillary surface waves on fluid-fluid interfaces," Biomicrofluidics **4**, 026501 (2010).

[72] O. Lioubashevski, H. Arbell, and J. Fineberg, "Dissipative solitary states in driven surface waves," Phys. Rev. Lett. **76**, 3959 (1996).

[73] L. Menguy and J. Gilbert, "Non-linear acoustic streaming accompanying a plane stationary wave in a guide," Acustica **86**, 249 (2000).

[74] J. W. S. Rayleigh, *Theory of Sound* (Dover, Toronto, 1945), Vol. 2.

[75] P. J. Westervelt, "The theory of steady rotational flow generated by a sound field," J. Acoust. Soc. Am. **25**, 60 (1953).

[76] S. J. Lighthill, "Acoustic streaming," J. Sound Vib. **61**, 391 (1978).

[77] G. Falkovich, A. Weinberg, P. Denissenko, and S. Lukaschuk, "Floater clustering in a standing wave," Nature (London) **435**, 1045 (2005).